Stability and Control Investigations of Generic 53 Degree Swept Wing with Control Surfaces

Andreas Schütte* and Kerstin C. Huber†
DLR, German Aerospace Center, D-38108 Brunswick, Germany
Neal T. Frink‡
NASA Langley Research Center, Hampton, Virginia 23681
and
Okko J. Boelens§
National Aerospace Laboratory/NLR, 1059 CM Amsterdam, The Netherlands

DOI: 10.2514/1.C033700

A contribution for the assessment of the static and dynamic aerodynamic behavior of a generic unmanned combat air vehicle configuration with control devices using computational fluid dynamics methods is given. For the study, various computational approaches have been used to predict stability and control parameters for aircraft undergoing nonlinear flight conditions. For the computational fluid dynamics simulations, three different computational fluid dynamics solvers are used: the unstructured grid-based solvers DLR TAU code and USM3D from NASA, as well as the structured grid-based National Aerospace Laboratory/NLR solver ENSOLV. The numerical methods are verified by experimental wind-tunnel data. The correlations with experimental data are made for static longitudinal/lateral sweeps and at varying frequencies of prescribed roll/pitch/yaw sinusoidal motions for the vehicle operating with and without control surface deflections. Furthermore, the investigations should support the understanding of the flow physics around the trailing-edge control devices of highly swept configurations with a vortex-dominated flowfield. Design requirements should be drawn by analyzing the interaction between the vortical flow and the control devices. The present work is part of the North Atlantic Treaty Organization's Science and Technology Organization/Applied Vehicle Technology Task Group AVT-201 on stability and control prediction methods.

Nomenclature

A	=	reference relation area, m^2
C_D	=	drag coefficient (aerodynamic coordinate system); $D/(q_\infty \cdot A)$
C_L	=	lift coefficient (aerodynamic coordinate system); $L/(q_\infty \cdot A)$
C_l	=	roll moment coefficient (aerodynamic coordinate system); $l/(q_\infty \cdot A \cdot s)$
C_m	=	pitch moment coefficient (aerodynamic coordinate system); $m/(q_\infty \cdot A \cdot c_{\text{ref}})$
C_{mx}, C_{MX}	=	roll moment coefficient (model fixed coordinate system); $M_x/(q_\infty \cdot A \cdot c_{\text{ref}})$
C_{my}, C_{MY}	=	pitch moment coefficient (model fixed coordinate system); $M_y/(q_\infty \cdot A \cdot s)$
C_{mz}, C_{MX}	=	yaw moment coefficient (model fixed coordinate system); $M_z/(q_\infty \cdot A \cdot s)$
C_n	=	yaw moment coefficient (aerodynamic coordinate system); $n/(q_\infty \cdot A \cdot s)$
C_p	=	pressure coefficient; $(p - p_\infty)/q_\infty$
C_S	=	side force coefficient (aerodynamic coordinate system); $s/(q_\infty \cdot A)$
C_y	=	side force coefficient (model fixed coordinate system); $F_y/(q_\infty \cdot A)$
C_z	=	normal force coefficient (model fixed coordinate system); $F_z/(q_\infty \cdot A)$
c_r	=	root chord, m
c_{ref}	=	reference length, m
f	=	Frequency, Hz
k_p	=	reduced frequency, pitch; $2\pi f \cdot c_{\text{ref}}/V_\infty$
k_R, k_Y	=	reduced frequency for roll and yaw; $2\pi f \cdot (b/2)/V_\infty$
$\log(r/r0)$	=	order of magnitude drop in solution residual: four example, -4 means a four-order-of-magnitude drop
M_∞	=	onflow Mach number
N_{cyc}	=	number of time steps per oscillation cycle, where the cycle is equal to $2\pi/(k \cdot \Delta t^*)$
p_∞	=	static pressure, N/m^2
q_∞	=	dynamic pressure; $0.5 \cdot \rho_\infty \cdot V_\infty^2$, N/m^2
rate1, rate2	=	primary and secondary VGRID "viscous" stretching factors; see Eq. (1)
T, Δt	=	time and physical time step, s
V_∞	=	onflow velocity, m/s
α, β	=	angle of attack and angle of sideslip, deg
Δt^*	=	characteristic time step; $\Delta t \cdot V_\infty/c_{\text{ref}}$
δ_{i+1}	=	VGRID viscous grid spacing normal to surface at node $i + 1$; see Eq. (1), m
δ_1	=	spacing of first node off of surface in viscous grid layers; see Eq. (1), m
η	=	flap deflection angle, deg
Θ, Θ_0, $\Delta\Theta$	=	pitch angle, nominal pitch, and pitch amplitude, deg
ρ_∞	=	density, kg/m^3
Φ, Φ_0, $\Delta\Phi$	=	roll angle, nominal roll, and roll amplitude, deg
Ψ, Ψ_0, $\Delta\Psi$	=	yaw angle, nominal yaw, and yaw amplitude, deg

Presented as Paper 2014-2133 at the 32nd AIAA Applied Aerodynamics Conference, Atlanta, GA, 16–20 June 2014; received 3 September 2015; revision received 9 December 2015; accepted for publication 11 December 2015; published online 29 March 2016.

*Research Scientist, DLR Institute of Aerodynamics and Flow Technology, Lilienthalplatz 7; andreas.schuette@dlr.de. Senior Member AIAA (Corresponding Author).

†Research Scientist, DLR Institute of Aerodynamics and Flow Technology, Lilienthalplatz 7; kerstin.huber@dlr.de.

‡Senior Researcher, Configuration Aerodynamics Branch, Research Directorate, MS 499; neal.t.frink@nasa.gov. Associate Fellow AIAA.

§RandD Engineer, Applied Computational Fluid Dynamics, Department of Flight Physics and Loads, Aerospace Vehicles Division; okko.boelens@foi.se.

I. Introduction

THE understanding and prediction of the flow physics, as well as the stability and control behavior, of modern fighter-type configurations at medium and high angles of attack (AOAs) are key to achieving superior maneuverability and performance. Recent unmanned combat air vehicle (UCAV) configurations and design studies used medium to highly swept wings with round or variable leading-edge (LE) geometries. The performance and signature considerations often result in medium leading-edge sweep angles of 45–60 deg. The design constraints of future agile and low observable UCAV configurations are a compromise between a minimum cross section and an advanced flight performance to achieve long range with remaining agility.

The planform can vary from a pure delta to a diamond, and even a lambda wing configuration. All of these configurations are more or less blended wing/bodies with a relatively small thickness ratio of the inner wing/fuselage part. The aerodynamics of these configurations is characterized by a nonlinear aerodynamic behavior dominated by a complex vortical flowfield on the upper side of the wing. The progression of these vortices depends on the sweep angle, the leading-edge geometry, the planform shape, and the onflow conditions, such as angle of attack, Mach number, and Reynolds number.

The challenge of the design is to achieve high agility and flight performance without any vertical tail plane to avoid the increase of the radar cross section. All control forces and moments should be provided by control effectors that do not significantly alter the radar cross section at all or only at points in the flight envelope where no threat could appear during takeoff, landing, or outside of the operating range. As long as no unconventional control devices are available, it is necessary to look at conventional trailing-edge devices for pitch, roll, and yaw control motion. For flight conditions at small angles of attack, these conventional trailing-edge devices work quite well, as applied in several configurations like the Boeing B2 aircraft. For medium to high angles of attack with a vortical flowfield on the upper wing of the configuration, these kinds of control surface setups might not work or are less efficient as in flight regimes with fully attached flow.

The understanding and prediction of the flow physics of delta wing configurations with round or variable leading edges are still challenging. Within the North Atlantic Treaty Organization (NATO) Science and Technology Organization (STO)/Applied Vehicle Technology (AVT) Panel Task Groups, several configurations have been tested in the wind tunnel and numerical investigations have been performed to predict the overall flight physics and stability and control coefficients. The progression and location of the vortical flow around delta wings with round leading edges have been investigated in Vortex Flow Experiment 2 (VFE-2) within the NATO Research and Technology Organization (RTO)/AVT-113 Task Group [1–3]. The flow around a 65 deg delta wing with sharp and round leading edges is analyzed by an integrated approach of experimental wind-tunnel tests and numerical simulations. Among others, numerical results using the DLR TAU code have been described by Schütte and Lüdeke [4] and summaries of lessons learned were given by Fritz and Cummings [5], as well as by Luckring and Hummel [6]. All results are published in the RTO Final Report by Hummel et al. [7]. The result of the VFE-2 was a basic understanding of the vortical flow structure and aerodynamics of delta wing configurations with round leading edges. The report also laid out the prediction capability with computational fluid dynamics (CFD) methods in comparison to experimental data, as well as limitations regarding the prediction of the complex aerodynamics with CFD methods.

A second configuration within the AVT-113 Task Group was a real fighter-type configuration, the F-16 Cranked Arrow Wing Aerodynamics Project International (CAWAPI), which was simulated with CFD Reynolds-averaged Navier–Stokes (RANS) methods as well. The results were published in the final report of AVT-113 [7] and, among others, by Boelens et al. [8], Görtz et al. [9], and Fritz et al. [10] In addition, in the work by Schütte et al. [11], results performed in the framework of the AVT-161 Task Group were simulating the X-31 configuration in comparison to experimental wind-tunnel data. Several results were presented using the DLR TAU and ENSOLV RANS CFD codes for both applications: the X-31 and the CAWAPI F-16XL configurations.

Within the AVT-161 Task Group, the planform of the current UCAV configuration called the stability and control, or SACCON, configuration was developed. In AVT-161, the stability and control prediction capabilities using CFD methods have been investigated for the configuration without control devices. The research group provided an extended experimental database for computer code validation purposes [12,13] to analyze the flow physics and aerodynamic, behavior, as well as the stability and control parameters. The results are presented in the final report of the AVT-161 Task Group [14]. The objectives and strategy of the research group were described by Cummings et al. [15]. A detailed description of the flow physics and evaluation of the stability and control prediction capabilities of the SACCON configuration was given by Schütte et al. [16] and Frink et al. [17].

In the follow-on program within the NATO STO/AVT-201 Task Group on extended stability and control prediction methods for NATO air vehicles [18,19], the SACCON UCAV configuration was modified, and trailing-edge control devices were implemented. A description of the model configurations and experimental results from the wind-tunnel tests were presented for the low-speed tests by Huber et al. [20] and Vicroy et al. [21] and for the high-speed investigations by Rein et al. [22].

In this paper, the prediction capabilities of high-fidelity, Reynolds-averaged Navier–Stokes-based CFD methods of the flowfield and aerodynamic behavior of the SACCON configuration with control devices will be shown. The paper starts with the prediction of the flow physics of the clean baseline (BL) configuration (no flap deflection) followed by a comparison between different control surface settings and the BL configuration without flap deflection. The differences between the numerical simulations and experimental data will be discussed, as well as sensitivities regarding the numerical approach, the CFD method, and applied turbulence models. Finally, comparisons between numerical and experimental simulations of dynamic pitch maneuvers will be presented and discussed.

II. Unmanned Combat Air Vehicle Model Configuration and Experimental Approach

The DLR-F19 configuration is part of a model family based on the geometry of the generic UCAV configuration SACCON developed within NATO STO/AVT research activities. The DLR-F19 configuration, as shown in Fig. 1, has control surfaces located on the left- and right-hand sides along the trailing edge of the outer wings and at the wingtips. The related model without control devices based on the same geometry is the SACCON or DLR-F17 model [12].

The hinge line of the trailing-edge control surfaces is located at 75% of the outer wing chord c_{ref}, and the control surface deflections for all control surfaces taken into account are $\eta = -20$, 0, and $+20$ deg. The reference geometry parameters are shown in Fig. 2. For the Reynolds number and the pitching moment, the reference length is the outer wing chord c_{ref} and, for the rolling and yawing

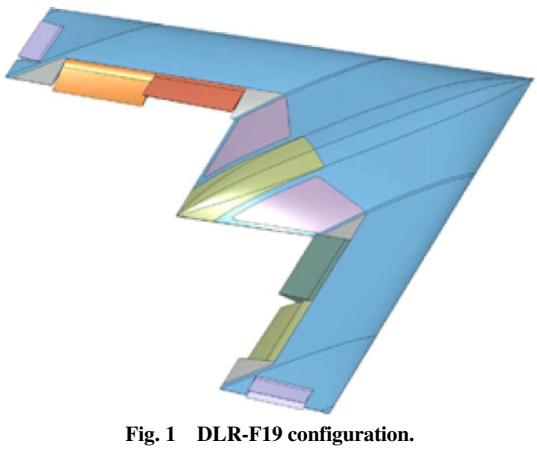

Fig. 1 DLR-F19 configuration.

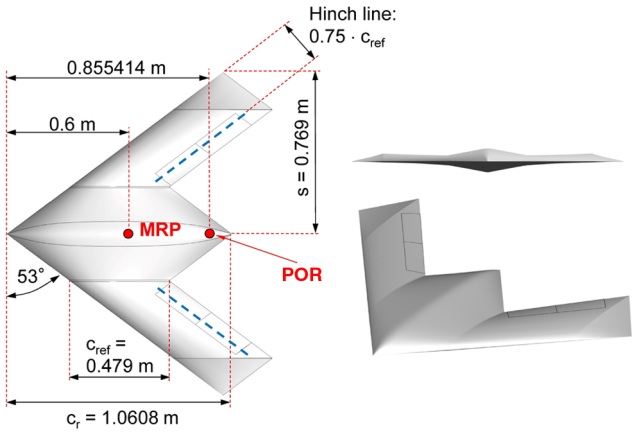

Fig. 2 Reference geometry parameters for the DLR-F19 configuration.

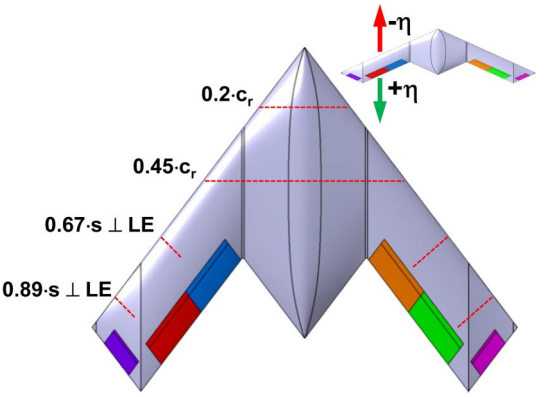

Fig. 4 Position of the pressure ports and sign convention for the deflection of the control surfaces.

moments, is the half-span s. The point of rotation (POR) for the static and dynamic measurement is located where the belly sting support is connected to the lower rear part of the model. All forces and moments are related to the moment reference point (MRP) at $x = 0.6$ m. A detailed description of the design process from the BL SACCON configuration to the DLR-F19 with control devices was given by Liersch and Huber [23].

Static and dynamic forces, moments, and surface pressure measurements have been performed in the German–Dutch Wind Tunnels (DNW-NWB) [24] low-speed wind-tunnel facility in Brunswick with the DLR-F19 configuration. The measurement data are averaged over a time period of 2 s. In several plots in the following sections, the amplitude of the measured data points are indicated by vertical bars. The wind-tunnel tests have been performed in the closed test section, and the model was mounted on a belly sting support located on the lower side of the model, as depicted in Fig. 3. The belly sting support was mounted on a six-degree-of-freedom (6-DOF) model positioning mechanism set up within the DNW-NWB to allow for maneuver simulations within the wind tunnel [24].

Figure 4 shows the location of the pressure ports on the upper and lower sides of the model, as well as the sign convention of the control surface deflections.

For comparisons between the numerical simulations and experiments, a common static and dynamic test case matrix was defined in cooperation with the STO/AVT-201 Task Group. The matrix contains test cases for the baseline configuration in comparison with cases where control surface deflections have been established. Both static and dynamic pitch and yaw maneuvers have been defined. A detailed description of the experiments and experimental results presented in this paper can be found in work by Huber et al. [20] and Vicroy et al. [21].

III. Numerical Approach

Within the paper, three different computational RANS methods have been applied. The DLR TAU code based on a cell-vertex scheme using hybrid computational grids, the National Aerospace Laboratory/NLR (NLR) CFD solver ENSOLV based on a cell-centered scheme using a structured computational grid approach, and the NASA CFD solver USM3D based on a cell-centered scheme using unstructured tetrahedral grids.

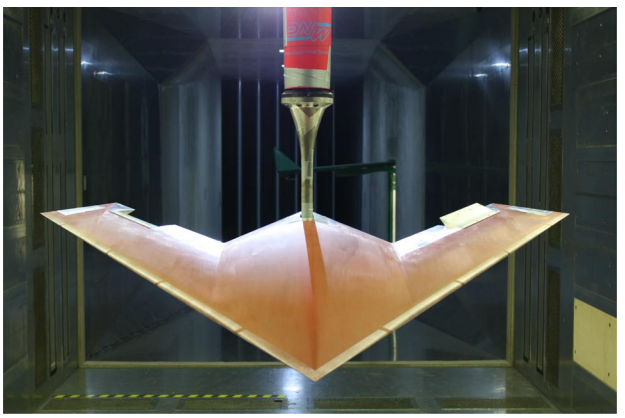

Fig. 3 DLR-F19 generic UCAV wind-tunnel model with trailing-edge control devices. Belly sting support is on the lower rear side of the model.

A. DLR Flow Solver TAU

One flow solver used in the present paper is the DLR TAU code: a CFD software developed by the DLR Institute of Aerodynamics and Flow Technology [25–28]. The TAU code solves the compressible three-dimensional time-accurate Reynolds-averaged Navier–Stokes equations using a finite volume formulation. The code is based on a hybrid unstructured-grid approach to be able to handle structured and hybrid computational grids, which makes use of the advantages offered by prismatic grid structures applied to resolve the viscous shear layer close to the wall and the flexibility in grid generation offered by unstructured grids.

The compressible equations in the TAU code in full conservation form are discretized in space by a second-order-accurate finite volume method. The TAU code basic version uses a cell-vertex metric with a dual-grid approach in order to make the flow solver independent from the cell types used in the initial grid. Within the TAU code, a typical Jameson-type matrix dissipation and several upwind schemes can be used. For the current applications in all simulations, the matrix dissipation has been applied.

The TAU code consists of several different modules. One of these modules is the motion module, which allows generation of any kind of rigid-body motion as well as relative motion between different parts of the computational models. The motion can be described by polynomial and Fourier functions, as well as by motion files provided by Python-based interfaces.

The current simulations have been performed using the steady-state and unsteady dual time-stepping approaches. The dual time-stepping approach was used for the dynamic maneuver simulations as well as for steady-state simulations by averaging over a certain time period. The latter was always applied in cases where no steady-state solution could be achieved.

For the numerical simulations, two physical RANS models have been used. A first approach uses a version of the one-equation Spalart–Allmaras (SA) turbulence model [29], referred to as SA-neg. The SA-neg version allows particularly negative values of the transport turbulence quantities [30]. This modification should lead to a more efficient solution of the equation without changing the dedicated aerodynamic solution.

The main turbulence model used for the TAU code simulations is a Reynolds-stress turbulence model (RSM) [31,32]. The RSM actually applied is a modified SSG/LLR-ω model with a different formulation of the length scale variable ω transferred to $g = 1/\sqrt{\omega}$. This transformation should provide a more stable solution close to the wall that leads to a reduced dependency of the computational grid at the wall. A first idea of this transformation can be found in publications by Kalitzin [33] and Kalitzin and Iaccarino [34].

Table 1 Computational grid dimensions and configurations (DLR-TAU simulations)

	LOB η, deg	LIB η, deg	RIB η, deg	ROB η, deg	No. of grid points	No. of elements	No. of prism layers
BL	0	0	0	0	43.3×10^6	105.6×10^6	30
LIB/RIB	0	−20	+20	0	42.6×10^6	102.2×10^6	30
LOB/ROB	−20	0	0	+20	42.2×10^6	101.4×10^6	30
LOBLIB/RIBROB	−20	−20	+20	+20	42.6×10^6	102.6×10^6	30
LOBLIB	−20	−20	0	0	42.3×10^6	101.8×10^6	30

In the following, the two specific turbulence model versions for the DLR TAU code will be abbreviated as SA and RSM, respectively.

B. NLR Flow Solver ENSOLV

The flow solver ENSOLV, which is part of the NLR's in-house developed flow simulation system ENFLOW [35,36], is capable of solving the Euler, RANS, large-eddy simulation (LES), and hybrid RANS/LES (extra-large-eddy simulation) equations on multiblock structured grids for arbitrary configurations. The configuration can be either fixed or moving relative to an inertial reference frame, and it can be either rigid or flexible. The compressible equations in full conservation form are discretized in space by a second-order-accurate cell-centered finite volume method using multiblock structured grids, central differences, and matrix artificial diffusion. The artificial diffusion consists of a blending of second-order and fourth-order differences with a Jameson-type shock sensor for the basic flow equations and a total variation diminishing discontinuity sensor for the turbulence model equations.

The current simulations have been performed as steady flow simulations, for which the discretized time-dependent system of equations is integrated toward the steady-state solution using a five-stage explicit Runge–Kutta scheme. Local time-stepping and multigrid acceleration techniques are applied.

Several turbulence models are present in the flow solver ENSOLV, including the turbulent nonturbulent k-ω model [37,38], the explicit algebraic Reynolds-stress model (EARSM), and a subgrid model for simulation using the hybrid RANS/LES equations for extra-large-eddy simulation [39,40]. The simulations presented in this paper have been performed employing the EARSM.

C. NASA Flow Solver USM3D

The computations are performed with USM3D [41], which is a parallelized tetrahedral cell-centered finite volume Navier–Stokes flow solver. The term "cell centered" means that the finite volume flow solution is solved at the centroid of each tetrahedral cell. Inviscid flux quantities are computed across each tetrahedral cell face using various upwind schemes. Spatial discretization is accomplished by a novel reconstruction process, based on an analytical formulation for computing solution gradients within tetrahedral cells. The solution can be advanced in time by a second-order "physical" time-step scheme, a second-order "dual" time-step scheme, or to a steady-state condition by an implicit backward-Euler scheme. Several turbulence models are available: the Spalart–Allmaras one-equation model, the two-equation k-ε turbulence model, the Menter shear stress transport (SST) two-equation model, and the nonlinear algebraic Reynolds-stress models of Girimaji [42] and Shih et al. [43]. For generalized grid motion, the USM3D flow solver has been installed as a plug-in to the fluid dynamics/computational analysis of dynamically responsive environments (FD-CADRE) framework [44] developed at the Arnold Engineering Development Center in Tullahoma, Tennessee. FD-CADRE is a generalized dynamic process control manager for coupling various plug-ins, e.g., flow solver, 6-DOF motion generator, aeroelastic structural module, etc. The latest extensions to the USM3D flow solver were described by Pandya et al. [45].

D. Computational Grids

1. *Hybrid Grids (DLR TAU Code)*

The hybrid unstructured grids used for the simulations with the DLR TAU code have been created with the hybrid grid generator Centaur, developed by CentaurSoft [46]. Table 1 lists the different cases to be discussed in this paper by using the CFD solver DLR TAU code. The belly sting support has been taken into account for most of the cases. In simulations where this is not the case, it will be explicitly pointed out in the text.

Figure 5 shows an example of the grid topology for the left outboard trailing-edge flap (LOB)–left inboard trailing-edge flap (LIB)/right inboard trailing edge flap (RIB)–right outboard trailing-edge flap (ROB) case, also referred to as LOBLIB/RIBROB. The prismatic layer and the further refinement of the tetrahedral grid in the field can be seen. This refinement based on an approximation of the element size compared to vortex size is done using a field source and increases the grid resolution in the area above the upper wing where the vortices appear. The grid topology and refinement ARE done in the same way for all computational grids. Figure 6 shows the prismatic layer in the vicinity of the deflected control surface, as well as the surface triangulation on the control device (denoted by the label "Surface triangles"). Looking at the numbers in Table 1, it can be seen that the differences of the control device setting cause only small differences in the overall number of grid points and elements. For all hybrid grids, the spacing of the first prismatic layer normal to the wall is $\delta_1/c_{\text{ref}} = 1.04\text{E}-05$, resulting in a typical $y+$ value of approximately one. The boundary layer is fully resolved by 30

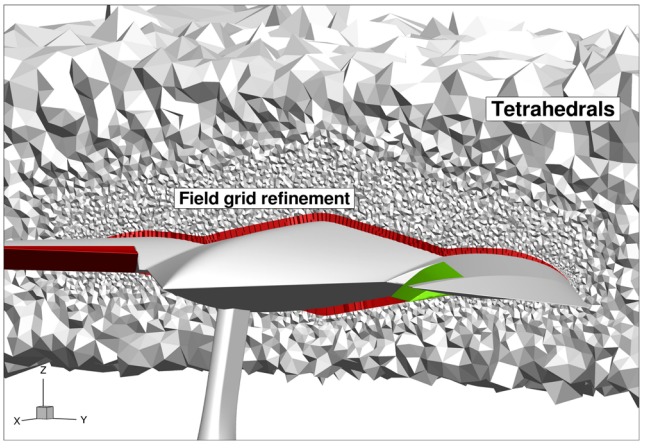

Fig. 5 Hybrid unstructured grid with the prismatic layer and the tetrahedral field mesh, including grid refinement area.

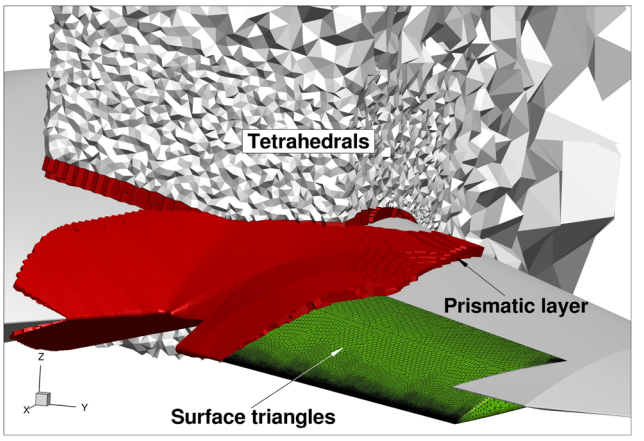

Fig. 6 Detailed view of the prismatic layer, the tetrahedral field mesh, and triangulation of the control devices on the right-hand side.

prismatic layers. Over the entire surface of the configuration, the full 30 prismatic layers can be achieved with no chopping of the layers. To generate the grids, two approaches are applied. For all grids taking the belly sting into account, a remeshing for all control surface (CS) deflections have been used. If the sting is not applied, a modular grid approach is used. In this case, the background grid was generated for one side and mirrored to achieve a complete symmetry for the majority of the computational grid beside the CS area. The CS grid parts can be exchanged as modules, which are connected to the background grid using nonmatching boundaries.

2. *Structured Grids (NLR ENSOLV)*

The structured (multiblock) grids have been generated using NLR's Cartesian grid mapping technique [47–48]. The (semi-automatic) grid generation algorithms, based on a Cartesian grid mapping technique, have been developed at NLR and are part of the NLR's ENFLOW flow simulation system.

To enable the study of various control surface settings (i.e., the elevons) on the DLR-F19 configuration, a modular approach for the geometric modeling of the control surfaces is adopted. According to this method, the different independently moving parts of a configuration are contained in separate computational domains. The only requirement among these computational domains is that the boundary surfaces are connected properly. Different from standard methods, the grid points on the boundary surfaces do not have to match each other. The method is therefore also called the "nonmatching boundary" or "sliding boundary" method when relative motion between the domains exists. To allow communication between these computational domains, an interpolation method is applied on the nonmatching block boundaries.

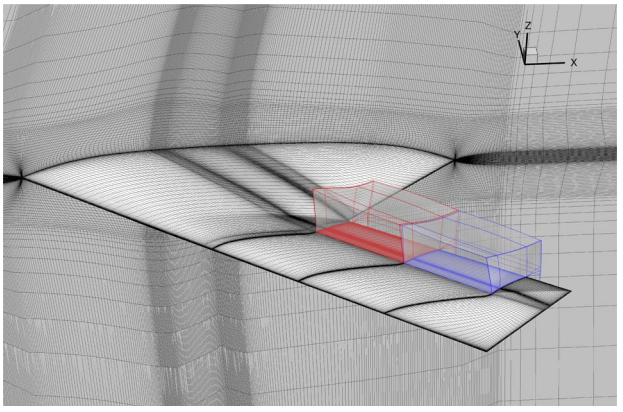

Fig. 7 Grid domains for the inner control surface (red) at $\eta = 0$ deg and the outer control surface (blue) at $\eta = 0$ deg (color in online only).

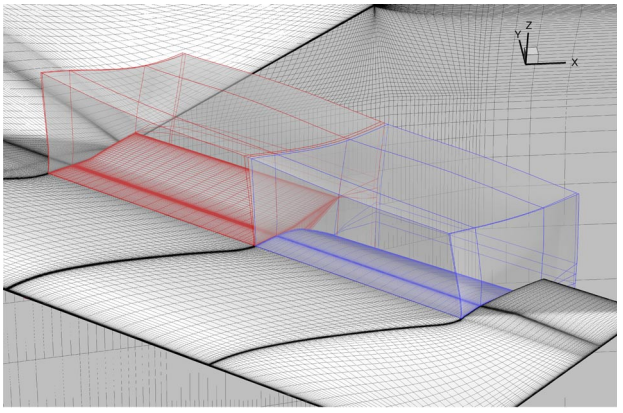

Fig. 8 Grid domains for the inner control surface (red) at $\eta = -20$ deg and the outer control surface (blue) at $\eta = 20$ deg (color in online only).

Table 2 Computational grid dimensions (NLR ENSOLV simulations)

	Short description	Number of blocks	Number of grid cells
Domain 1	DLR-F19 main body (half-configuration)	662	24,924,160
Domain 2	Inner control surface (elevon): $\eta = -20$, 0, and 20 deg	46	1,622,016
Domain 3	Outer control surface (elevon): $\eta = -20$, 0, and 20 deg	46	1,622,016

Figures 7 and 8 show the structured multi-block computational grids of the DLR-F19 half span configuration, where the following domains can be distinguished: 1) a domain containing the main body of the DLR-F19 configuration without the control surfaces; 2) a domain containing the inner control surface (elevon); and 3) a domain containing the outer control surface (elevon).

Note that this method requires a small gap between the solid surface of the main DLR-F19 body and that of the control surfaces, as well as between both control surfaces, to allow for a nonmatching boundary surface and a grid on both sides of this surface. For the domains with the control surfaces, grids have been generated at control surface settings where η equals −20, 0, and 20 deg. Initially, the domain containing the main body of the DLR-F19 configuration contains the half-configuration. The full-span configuration can be obtained by mirroring a half-span configuration and adding the two half-span configurations required using a nonmatching boundary at the configuration midplane.

Details on the grids can be found in Table 2. For these grids, the spacing of the first grid point normal to the solid wall is $\delta_1/c_{\text{ref}} = 1.04\text{E}-05$, resulting in a typical $y+$ value of approximately one.

3. *Tetrahedral Grids (NASA USM3D)*

A series of full-span tetrahedral grids were generated for the DLR-F19/F17 SACCON configurations shown in Fig. 9 using a developmental version of VGRID [49] and following guidelines developed by Frink [50]. Thin-layer tetrahedral grids were generated to meet requirements for cell-centered computations from the USM3D flow solver. A near-wall first-cell spacing was prescribed, based on flat-plate turbulent boundary-layer theory, to achieve a tetrahedral cell centroid turbulent wall coordinate y^+ of 0.5 at a longitudinal distance of $0.5^* c_{\text{ref}}$ for a Re_{cref} of 1.5 million. Since the VGRID advancing layers method marches nodes away from the vertices of the surface triangles (which are subsequently connected to form tetrahedral cells), an initial VGRID spacing δ_1, corresponding to a $y^+ = 2$ at the first node, was prescribed in order to achieve the $y^+ = 0.5$ at the first cell centroid. Subsequent USM3D computations confirmed that an average first-cell y^+ of approximately 0.4 was

Fig. 9 Grid 2 surface triangulations for DLR-F19 with CS0 and CS20, and DLR-F17 with aft sting. Left to right: G2.00, G2.20, and G2a.

Table 3 General full-span mesh properties for DLR-F19 with 15 deg yaw-link belly sting

Grid	LOB/LIB, deg	ROB/RIB, deg	VGRID *ifact*	Tetrahedra, millions	Nodes, millions	Wing triangles	Wing nodes
G1.00	— —	— —	1.9440	7.233	1.228	73,456	36,738
G2.00	— —	— —	1.4215	12.967	2.203	132,474	66,251
G3.00	— —	— —	1.0000	25.776	4.383	261,050	130,543
G1.20	−20/ − 20	+20/ + 20	1.9440	10.286	1.749	120,364	60,192
G2.20	−20/ − 20	+20/ + 20	1.4215	17.963	3.056	212,456	106,242
G3.20	−20/ − 20	+20/ + 20	1.0000	34.960	5.952	414,984	207,510

achieved. For the SACCON at the nominal wind-tunnel chord Reynolds number of 1.5 million, the required VGRID first-node spacing is $\delta_1/c_{\text{ref}} = 0.000024$, with primary and secondary stretching parameters set to rate $1 = 0.15$ and rate $2 = 0.02$, as defined in Eq. (1):

$$\delta_{i+1} = \delta_1[1 + \text{rate } 1(1 + \text{rate } 2)^i]^i \tag{1}$$

The same viscous spacing distribution was applied to all DLR-F19 and DLR-F17 grids and resulted in approximately 72 tetrahedral cells (24 nodes) across the boundary layer at the midchord of c_{ref}.

Six grids were generated on the DLR-F19 configuration with the 15 deg yaw-link post sting: coarse/medium/fine (G1/G2/G3), with and without flap deflections, with the characteristics listed in Table 3. Similarly, coarse/medium/fine grids were generated on the DLR-F17 with the aft roll sting producing the characteristics listed in Table 4. In both cases, the VGRID sources from the grids in [50] were transferred into the VGRID input files for the current configurations, thereby insuring a consistency with the prior study.

The upper surface grid triangulations for G1.20, G2.20, and G3.20 for the DLR-F19 with deflected control surfaces (referred to as CS20), along with corresponding volume grids slices through the right-wing control surface, are shown in Fig. 10. The grid refinement was achieved by changing the "*ifact*" parameter in the VGRID input, which globally scales the spacing for the "inviscid" portion of the grid, as highlighted in Fig. 10. The normal distributions across the viscous layers were not scaled in the process. Spanwise grid stretching with a ratio as high as 10-to-1 was applied along the leading and trailing edges for each G1, G2, and G3, as described by Frink [50], in order to reduce cell count. The additional detail of the surface and volume grids in the vicinity of the outboard gap for the right-wing control surface is provided in Fig. 11. The gap between abutting flap/wing surfaces was sealed.

Table 4 General full-span mesh properties for DLR-F17 with aft-roll sting

Grid	VGRID *ifact*	Tetrahedra, millions	Nodes, millions	Wing triangles	Wing nodes
G1a	1.9440	6.523	1.228	71,706	35,881
G2a	1.4215	11.689	1.987	130,048	65,059
G3a	1.0000	23.185	3.943	256,664	128,379

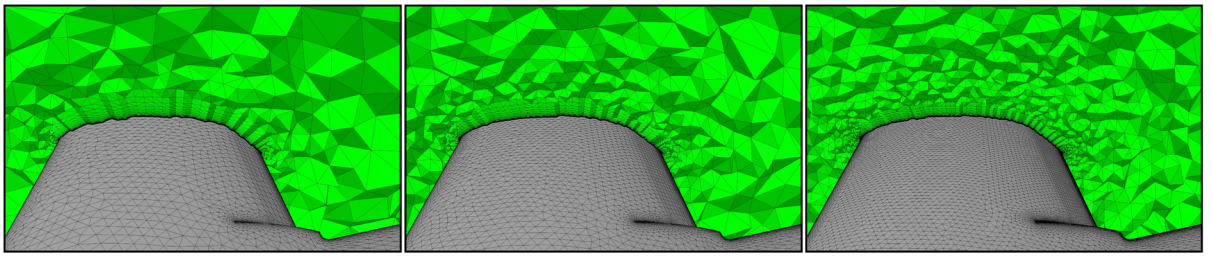

Fig. 10 Volume grid slices perpendicular to leading edge through right wing and deflected control surface for DLR-F19 CS20. Left to right: G1.20, G2.20, and G3.20.

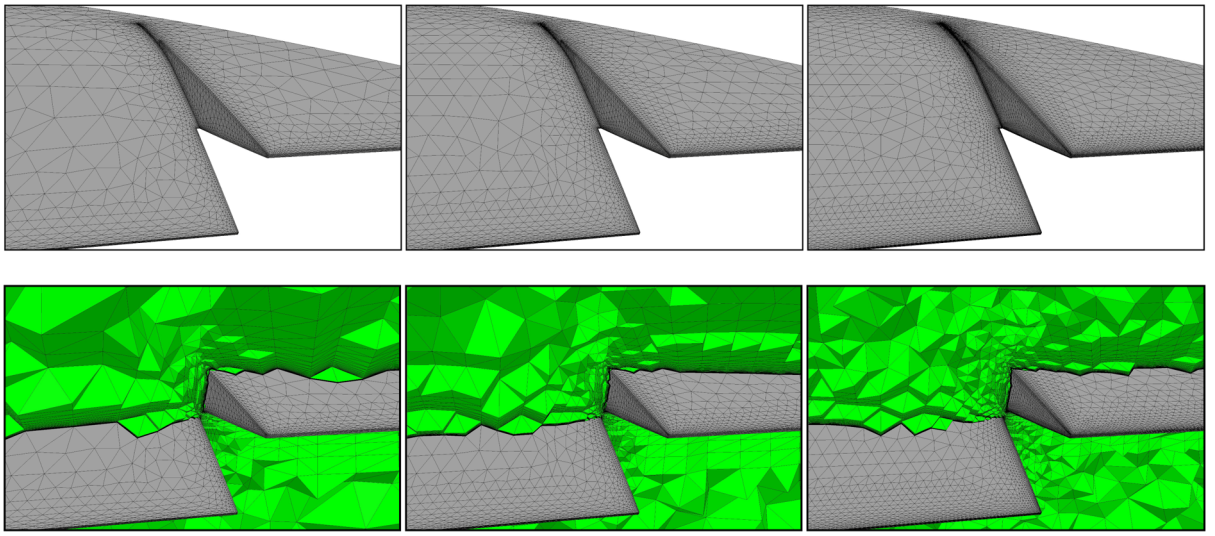

Fig. 11 Close-up of right wing outboard flap gap for DLR-F19 CS20: surface triangulation (top), and volume grid cut through control surface (bottom). From left to right: G1.20, G2.20, and G3.20.

Table 5 Integral data (at angle of attack of $\alpha = 10$ deg) obtained using NLR's flow solver ENSOLV

LOB η, deg	LIB η, deg	RIB η, deg	ROB η, deg		C_L	C_D	C_S	C_m	C_l	C_n
0	0	0	0	FS	0.1452	0.0330	0.0000	0.0281	0.0000	0.0000
				HSR	0.1452	0.0330	0.0000	0.0282	0.0000	0.0000
				Δ	0.0000	0.0000	0.0000	−0.0001	0.0000	0.0000
				Δ (%)	0.0	0.0	0.0	0.4	0.0	0.0
−20	−20	0	0	FS	0.3615	0.0301	0.0027	0.0438	−0.0334	−0.0052
				HSR	0.3612	0.0301	0.0051	0.0439	−0.0402	−0.0062
				Δ	0.0003	0.0000	−0.0024	−0.0001	0.0068	0.0010
				Δ(%)	0.1	0.0	88.9	0.2	20.4	19.2
−20	−20	20	20	FS	0.4129	0.0387	0.0027	0.0283	−0.0646	−0.0045
				HSR	0.4137	0.0390	0.0071	0.0272	−0.0796	−0.0063
				Δ	−0.0008	−0.0003	−0.0044	0.0011	0.0150	0.0018
				Δ(%)	0.2	0.8	163.0	3.9	23.2	40.0

IV. Computational Results

A. Baseline Configuration (DLR TAU Code)

First, the flow physics of the baseline configuration at symmetric and asymmetric onflow conditions will be discussed. The BL configuration is the reference case for all further discussions. In Figs. 12 and 13, the aerodynamic coefficients predicted by the DLR TAU code in comparison to the experiments are shown for two different turbulence models. The onflow Mach number, as for all following examples, is $M = 0.15$; and the Reynolds number is $Re_{\text{cref}} = 1.6 \times 10^6$. The flow physics and the resulting aerodynamic behavior were already described in detail by Schütte et al. [16]. However, some aspects should be discussed here again: the nonlinearity in the slope of the pitching moment around $\alpha = 15$ deg, and the prediction of the same coefficient at higher angles of attack beyond $\alpha = 18$ deg. The nonlinearity around $\alpha = 15$ deg is caused by a sudden movement of the tip vortex toward the apex along the leading edge. The huge dual-vortex structure causes a larger load aft of the MRP than in front of it, which results in the depicted dip of the pitching moment curve. At a higher AOA, the load distribution is moving toward the apex due to an increasing distance of the vortex system relative to the wing surface behind the MRP and by progressing vortex breakdown.

In the previous investigation using the SA turbulence model, it has been shown that the lift and drag, as well as the rolling moment, can be predicted quite well. For a higher AOA, however, the one-equation model is not able to predict the vortex breakdown and structure correctly and the suction peaks caused by the vortices on the upper surface are overpredicted, and hence are too strong. Higher-order turbulence models have to be applied to be able to predict the flow physics better. In Fig. 13, the RSM turbulence model is applied, and it can be seen that the overestimated pitching moment for an AOA higher then $\alpha = 18$ deg is still existent in comparison to the SA results but on a lower level. This aspect will be discussed again regarding the pressure distribution and flow topology.

Both approaches underestimate the pitching moment at a lower AOA. One reason might be caused by the complex wake flow of the sting, which is not predicted correctly either.

Figures 14 and 15 show the pressure distribution at angles of attack of $\alpha = 14$ and 18 deg. With respect to the upper side of the configuration, the prediction of the surface pressure distribution matches qualitatively well for both turbulence models. However, it can be seen that the SA turbulence model overestimates the pressure suction peaks of the apex vortex largely. Even though the integral data match better using the SA rather than the RSM approach, the related pressure distribution is significantly off.

Figure 15 shows the reason for the overestimated pitching moment for both cases beyond an AOA of 18 deg. For the SA approach, it is caused by the overestimated suction of the apex vortex structure. This flow physics is much better represented by the RSM turbulence model. On the other hand, the pressure distribution in the tip area is underestimated due to an onset of vortex breakdown predicted too early.

Figures 16 to 19 show the corresponding flow topology on the upper side of the configuration. For $\alpha = 14$ and 18 deg, the typical vortical flow topology is predicted by both turbulence models. For $\alpha = 14$ deg, the tip vortex remains at the outer wingspan position and has moved toward the apex for $\alpha = 18$ deg. A difference between the two turbulence models can be observed comparing the

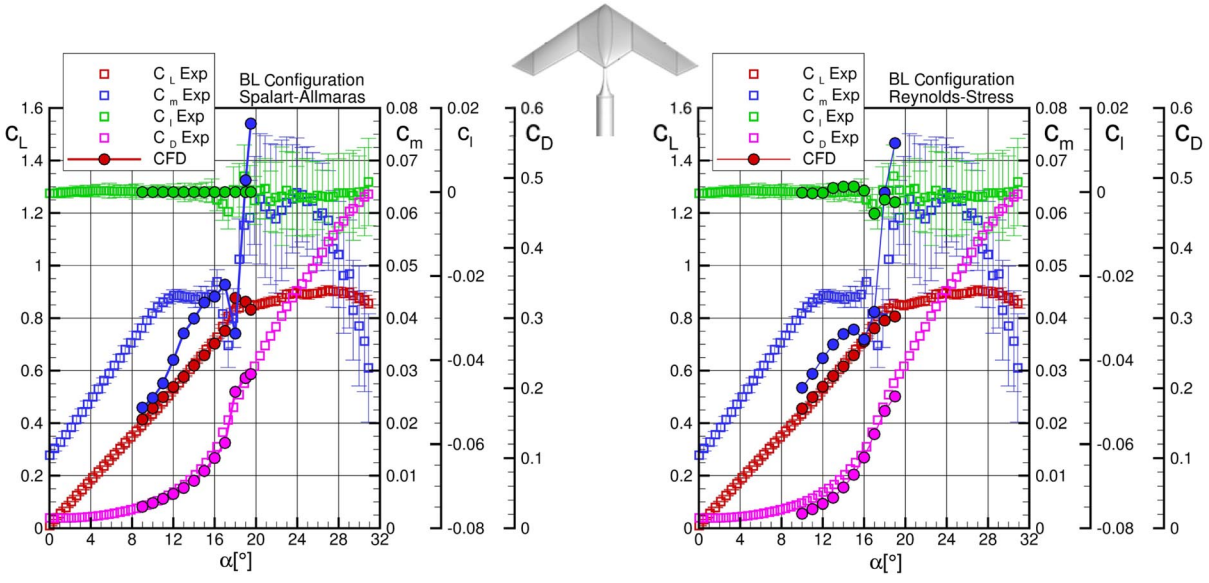

Fig. 12 Effect of turbulence model for BL configuration. DLR TAU code vs experiment. Lift, drag, pitching, and rolling moment coefficient.

Fig. 13 DLR TAU code prediction in comparison to the experiment using the Reynolds-stress turbulence model: lift, drag, pitching, and rolling moment coefficients.

vortex structure of the tip vortex for an AOA of $\alpha = 14$ deg. The SA model predicts a well-structured stable tip vortex; whereas for the RSM, an onset of vortex breakdown can be assumed, which actually causes the weaker suction peak at the wingtip, as depicted in Fig. 14 on the right side.

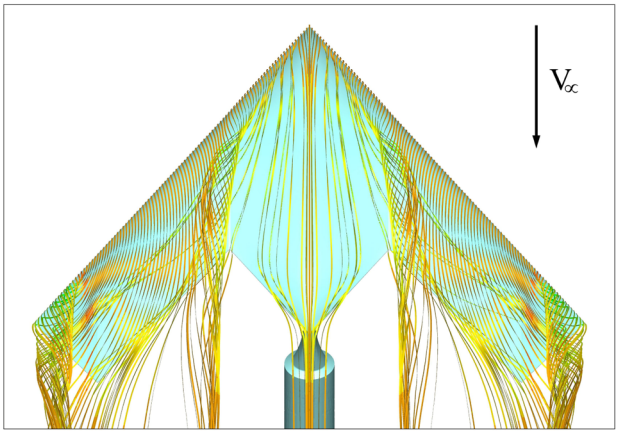

Fig. 16 Predicted flow topology on the upper side of the DLR-F19 configuration: $\alpha = 14$ deg, DLR TAU code (SA).

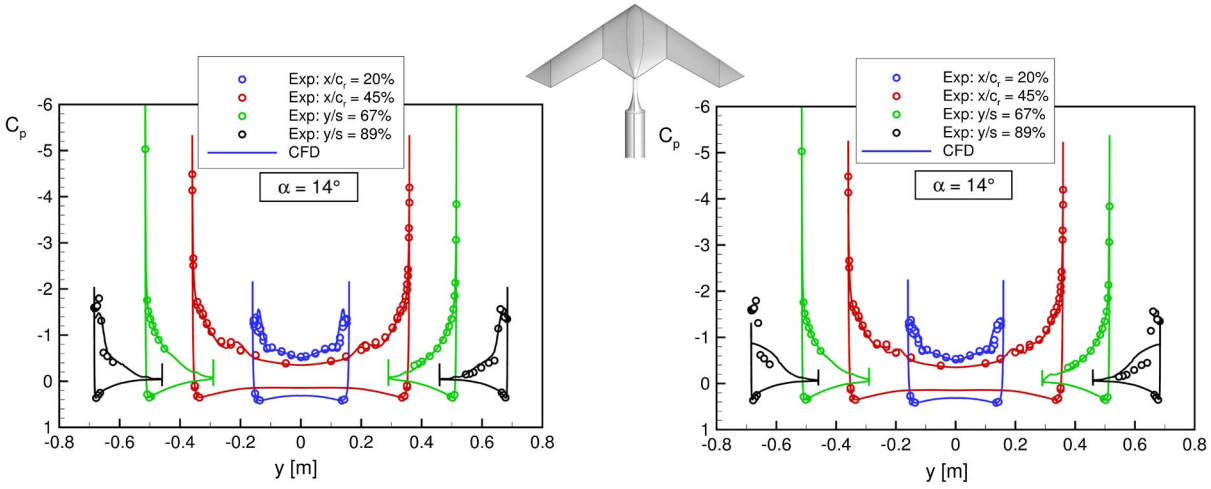

Fig. 14 Surface pressure distribution DLR TAU/Experiment at four different $x = \text{const.}$ locations: $\alpha = 14$ deg SA (left), and RSM (right).

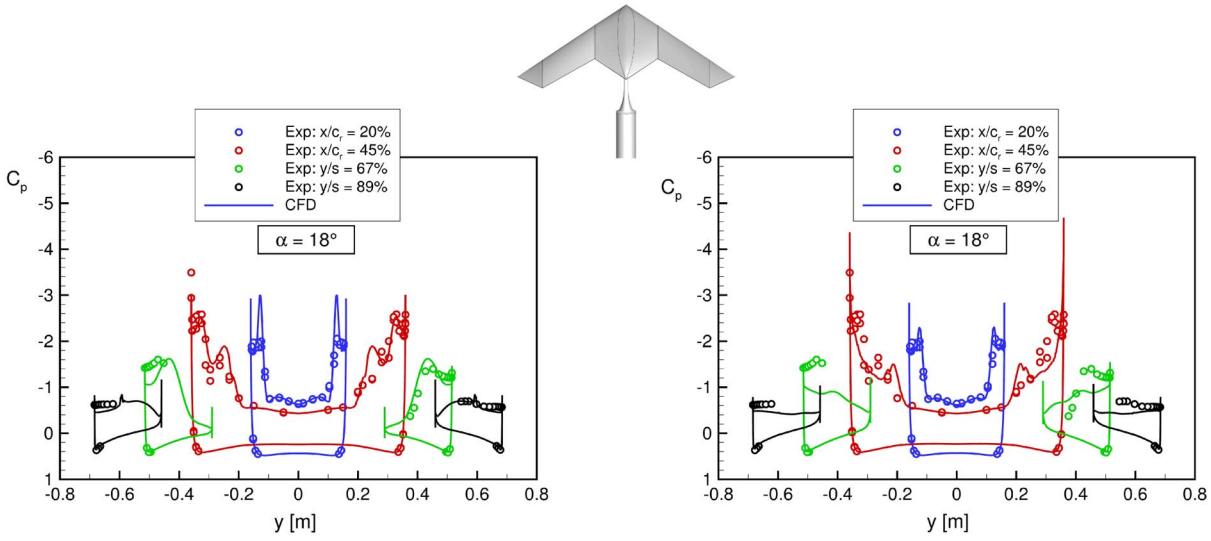

Fig. 15 Surface pressure distribution DLR TAU/Experiment at four different $x = \text{const}$ locations: $\alpha = 18$ deg SA (left), and RSM (right).

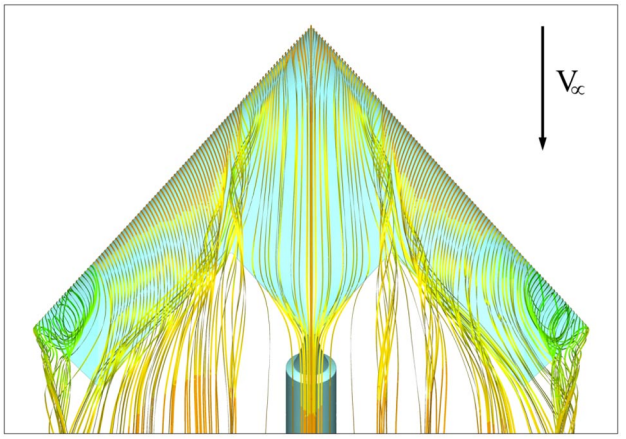

Fig. 17 Predicted flow topology on the upper side of the DLR-F19 configuration: $\alpha = 14$ deg, DLR TAU code (RSM).

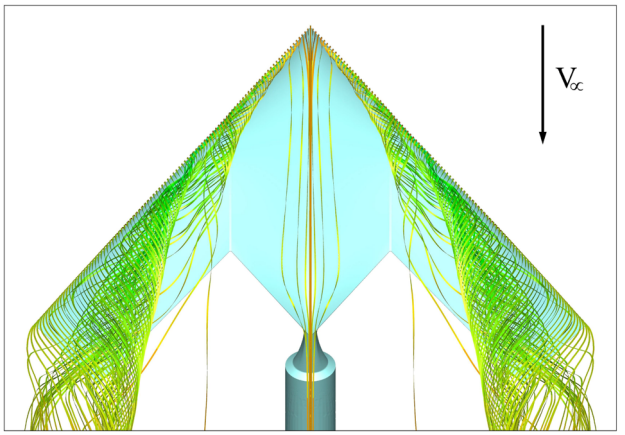

Fig. 18 Predicted flow topology on the upper side of the DLR-F19 configuration: $\alpha = 18$ deg, DLR TAU code (SA).

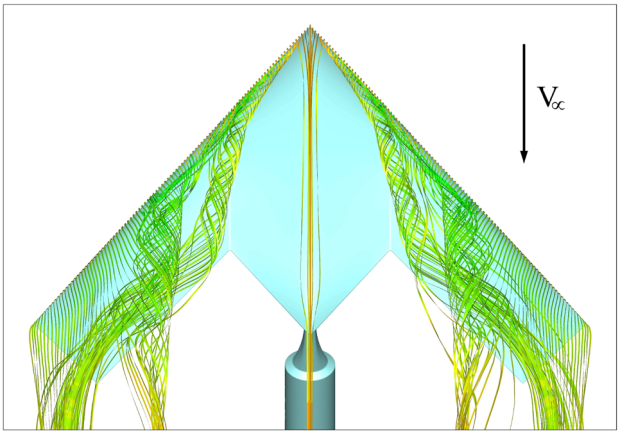

Fig. 19 Predicted flow topology on the upper side of the DLR-F19 configuration: $\alpha = 18$ deg, DLR TAU code (RSM).

For $\alpha = 18$ deg, a discrete two-vortex system occurs for the RSM turbulence model; whereas for the SA turbulence model simulation, the apex vortex is more or less collected by the huge second downstream vortex.

In comparison to the SA turbulence model solutions, the RSM approach does not deliver not more accurate results. However, it can be considered from previous investigations that, for the complex nonlinear flow physics, like vortex breakdown, higher-order turbulence models have to be applied. Consequently, the RSM

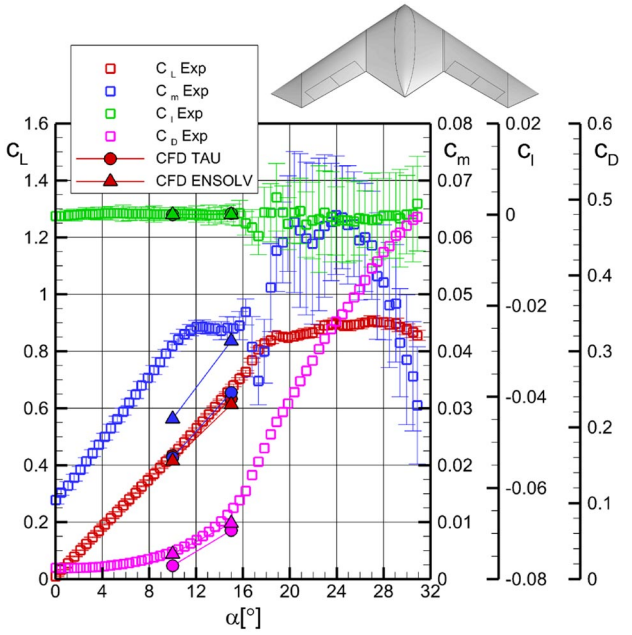

Fig. 20 BL configuration: DLR TAU code (RSM) and NLR ENSOLV (EARSM) (no sting) vs experiment (with sting).

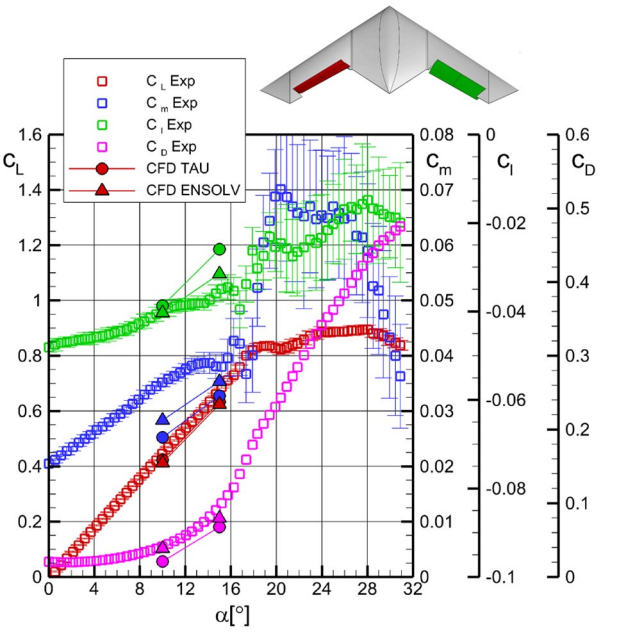

Fig. 21 LOBLIB/RIBROB configuration: DLR TAU (RSM) and NLR ENSOLV (EARSM) (no sting) vs experiment (with sting).

turbulence model will be applied in the following DLR TAU code simulations.

B. Control Surface Deflection (DLR TAU Code and NLR ENSOLV)

In the following section, the flow physics and aerodynamic stability and control parameter for the configurations with control surface deflection will be discussed. The reference for all comparisons is the BL configuration. In this section, symmetric onflow conditions apply.

First, the CFD results obtained by the DLR, German Aerospace Center (DLR) and the NLR for the full-span configuration without modeling the belly sting support will be shown. Next, a method to reconstruct the full-span integral data from the half-span integral data will be briefly

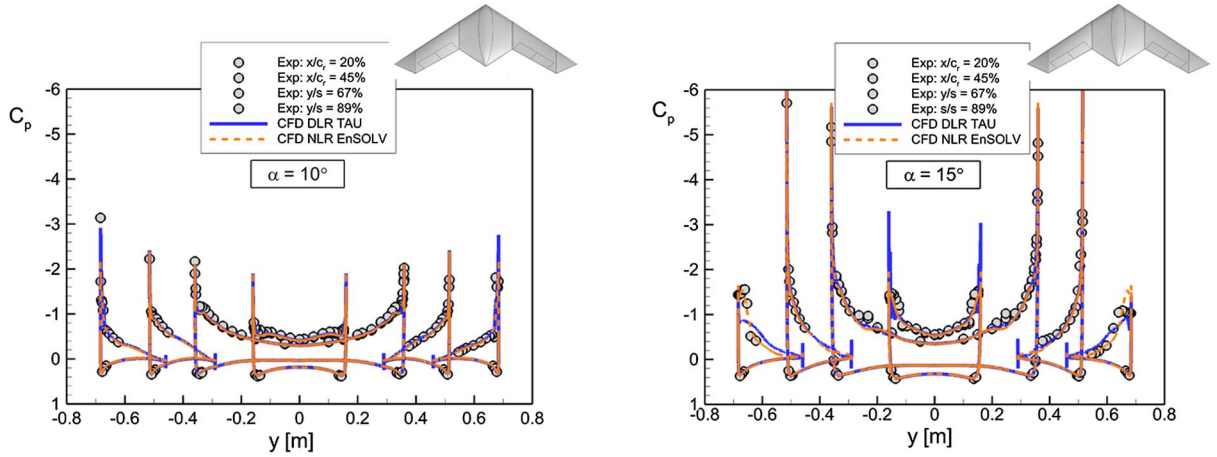

Fig. 22 BL configuration: surface pressure distribution DLR TAU (RSM) and NLR ENSOLV (EARSM) (no sting) vs experiment (with sting): $\alpha = 10$ and 15 deg.

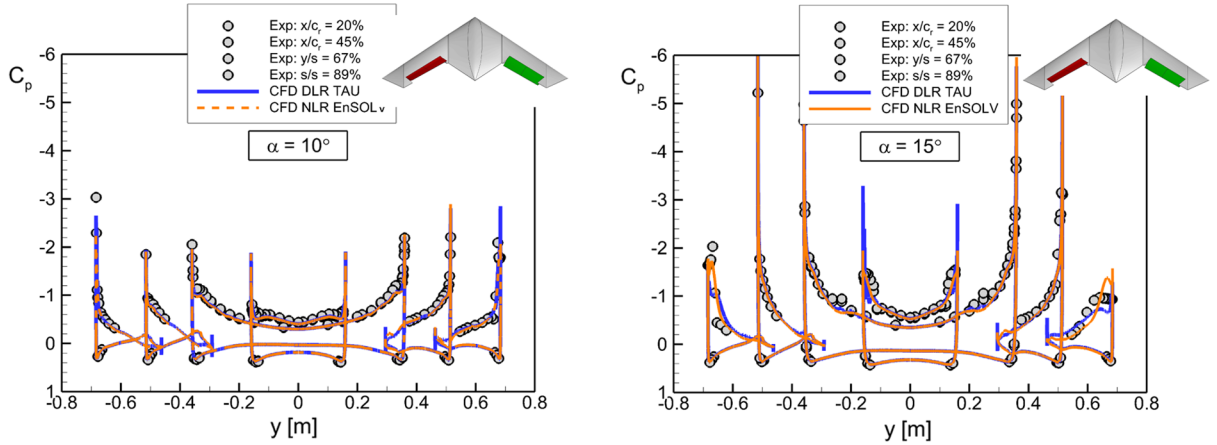

Fig. 23 LOBLIB/RIBROB configuration: surface pressure distribution DLR TAU (RSM) and NLR ENSOLV (EARSM) (no sting) vs experiment (with sting): $\alpha = 10$ and 15 deg.

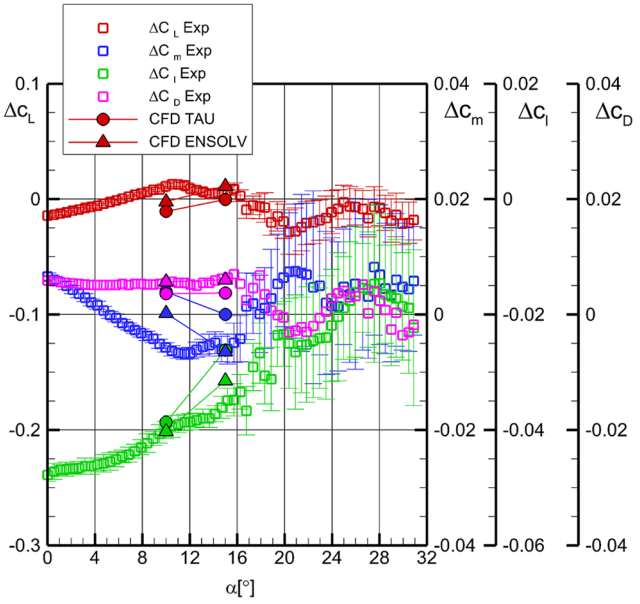

Fig. 24 LOBLIB/RIBROB versus BL configuration: DLR TAU (RSM) and NLR ENSOLV (EARSM) (no sting support) vs experiment (with sting support): $\alpha = 10$ and 15 deg.

discussed. Finally, a third section will elaborate on the result obtained at the DLR for the full-span configuration with the belly sting support.

1. *Symmetric Onflow Conditions: Full Span, No Sting*

The simulation results discussed in this section have been obtained using the DLR TAU code and NLR's flow solver ENSOLV on the grids discussed before, respectively. For these simulations, the full-span configuration without the belly sting support has been used. The DLR TAU code employs the Reynolds-stress turbulence model, whereas NLR's flow solver ENSOLV uses the explicit algebraic stress model.

In Figs. 20 and 21, the aerodynamic coefficients predicted by both CFD methods (at angles of attack of $\alpha = 10$ and 15 deg) in comparison to the experimental data are presented for two different control surface settings, i.e., the BL configuration in Fig. 20 and the LOBLIB/RIBROB configuration in Fig. 21. The results shown are completely in line with the results presented in Sec. IV.A. The absence of the belly sting support results once more in an underprediction of the pitching moment by both methods. Both methods predict the rolling moment coefficient C_l quite well, though the NLR ENSOLV is giving a slightly better prediction for this coefficient at $\alpha = 15$ deg.

Figures 22 and 23 show the corresponding pressure distributions for the BL configuration and the LOBLIB/RIBROB configuration, respectively, at angles of attack of $\alpha = 10$ and 15 deg in comparison to the experimental data. Although, for the BL configuration shown in Fig. 22, both the configuration and the flow conditions are fully symmetric, the experimental data show an asymmetry in the surface

pressure at the most rearward station ($y/s = 0.89$, perpendicular to the leading edge).

The agreement between both methods and the experiment is fairly good. Both methods underpredict the pressure suction peak from the apex vortex (at $x/c_r = 45\%$) and show a more inboard location of this vortex compared to the experiment. The pressure peak resulting from the leading-edge vortices seems in general to be better predicted by NLR's flow solver ENSOLV with the EARSM. The differences in the location and the strength of these suction peaks are the main reason for the differences in the integral forces.

Finally, in Fig. 24, the differences of the stability and control values between the configurations with (LOBLIB/RIBROB) and without (BL) control surface deflection are plotted against each other. Both methods show a fair agreement with the experimental data, indicating that such a differential approach may well be used for the purposes of stability and control database generation.

2. *Symmetric Onflow Conditions: Half-Span, No Sting*

Instead of simulating the full-span configuration at symmetric onflow conditions to obtain the integral data, these data may also be reconstructed from the half-span integral data. This means that the integral data of two half-span configurations representing the control surface deflections of a full-span configuration are added. The gain in doing so is mainly a reduction of the computing time and computing costs by a factor of two, however at the cost of possibly less accurate integral data, especially for configurations with asymmetric flap deflections.

Table 5 shows both the DLR-F19 full-span integral data (denoted by FS) as well as the reconstructed full-span integral data based on a series of half-span simulations (denoted by HSR) at an angle of attack of 10 deg. These data were obtained using NLR's flow solver ENSOLV.

The table clearly shows that, for the lift coefficient C_L, drag coefficient C_D, and pitching moment coefficient C_m, the agreement between both methods to obtain the integral data is very good. For the side force coefficient C_S, the rolling moment coefficient C_l, and the yawing moment coefficient C_n, the agreement is less satisfactory: especially the side force coefficient C_S shows a large discrepancy. It should, however, be noted that the absolute value of both the side force coefficient C_S and the yawing moment coefficient C_m is small compared to the other force and moment coefficients, and is therefore more prone to computational errors. Keeping these shortcomings in mind, it is clear that this approach provides a quick and reasonably accurate method for estimating the integral force and moment coefficients for symmetric onflow conditions early on in the process of stability and control database generation.

3. *Symmetric Onflow Conditions: Full Span, with Sting*

Figure 25 shows the DLR TAU code (RSM) results of the static aerodynamic coefficients for the BL and for the LOBLIB/RIBROB configuration in comparison to the experiment with no CS deflection. For the CS case, the simulations have only been done for AOAs of $\alpha = 10$ and 15 deg. The deflection of the control surfaces has no effect on the lift and almost no effect on the pitching moment. The rolling moment, however, has changed to negative values. Of additional note is that the effectiveness of the CS decreases with increasing AOAs.

In Fig. 26, the CS case DLR TAU code (RSM) results are plotted against the corresponding experimental data. It can be seen that the trend of a reduction of the rolling moment with a higher AOA is predicted correctly by the simulation; however, the CFD results predict a reduced effectiveness compared to the experiment. The CS deflections cause a counterclockwise turn of the configuration, which is underestimated by the CFD simulation represented by a less negative rolling moment.

Figures 27 and 28 show the experimental and simulated surface pressure distributions on the upper surface of the configuration without and with CS deflection at AOAs of $\alpha = 10$ and 15 deg. For both cases, the simulation fits quite well with the experiment, except for the flow physics in the wingtip area for $\alpha = 15$ deg. It is interesting to point out that, even for the BL configuration, small asymmetries occur. These asymmetries are also represented by the CFD simulations shown in Fig. 25, indicated by the asymmetries in the rolling C_l and yawing moments C_n.

Looking at the flow topology in Figs. 29 and 30, it can be seen that the tip vortex is not interacting directly with the flow over the control surfaces. The incorrectly predicted tip vortex flow probably has more effect on the pitching moment than the flow over the control surfaces. This is indicated by the pressure distribution in Fig. 28 on the right-hand side and the tip flow topology in Fig. 30 for $\alpha = 15$ deg (LOBLIB/RIBROB).

The suction peaks of the tip vortices in both cases are too low, as seen in Figs. 27 and 28. This causes a reduced load in the wingtip

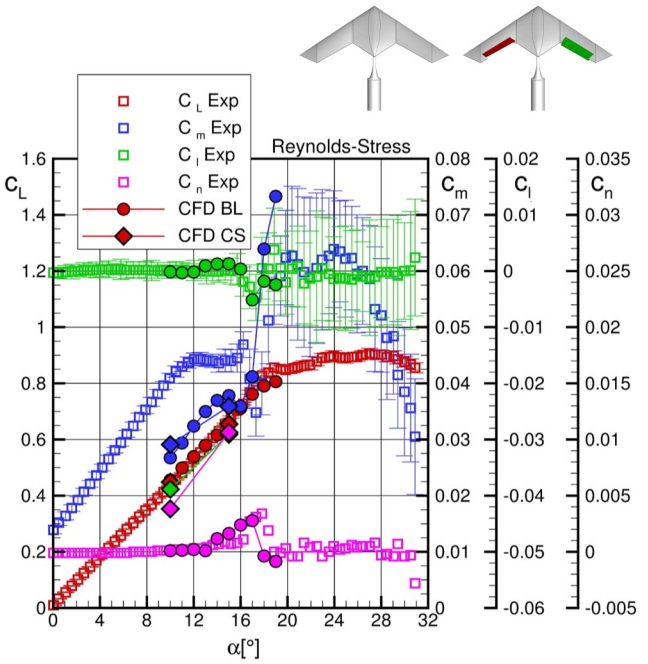

Fig. 25 Effect of CS deflection on rolling moment. DLR TAU (RSM) vs experiment: $\alpha = 10$ deg.

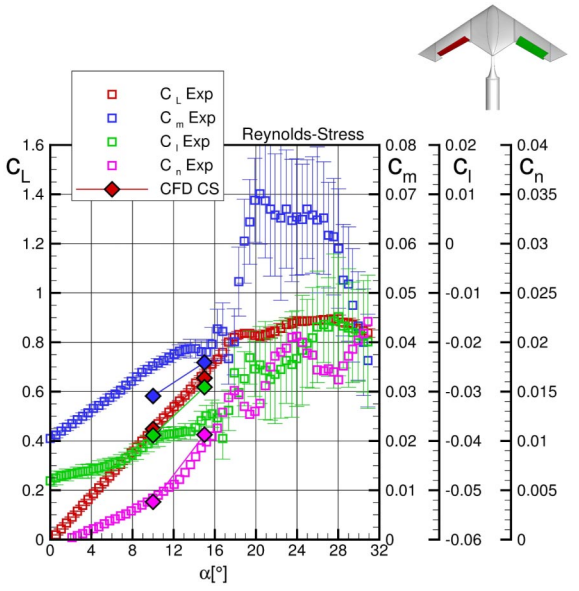

Fig. 26 CS configuration (LOBLIB/RIBROB). DLR TAU (RSM) vs experiment: lift, pitching, rolling, and yawing moment coefficients, $\alpha =$ 10 and 15 deg.

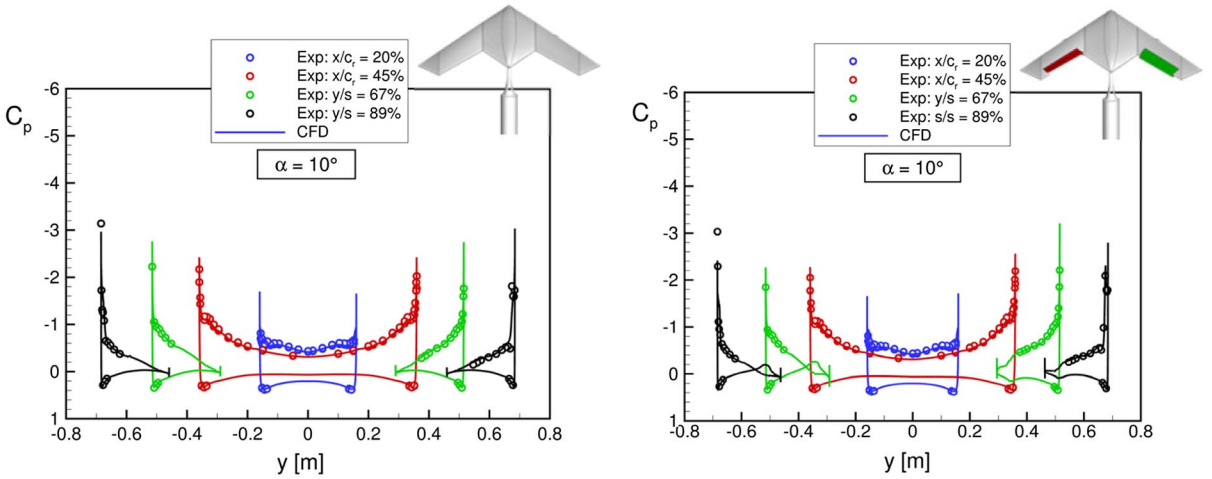

Fig. 27 BL and CS (LOBLIB/RIBROB) configuration: surface pressure distribution DLR TAU (RSM) vs experiment: $\alpha = 10$ deg.

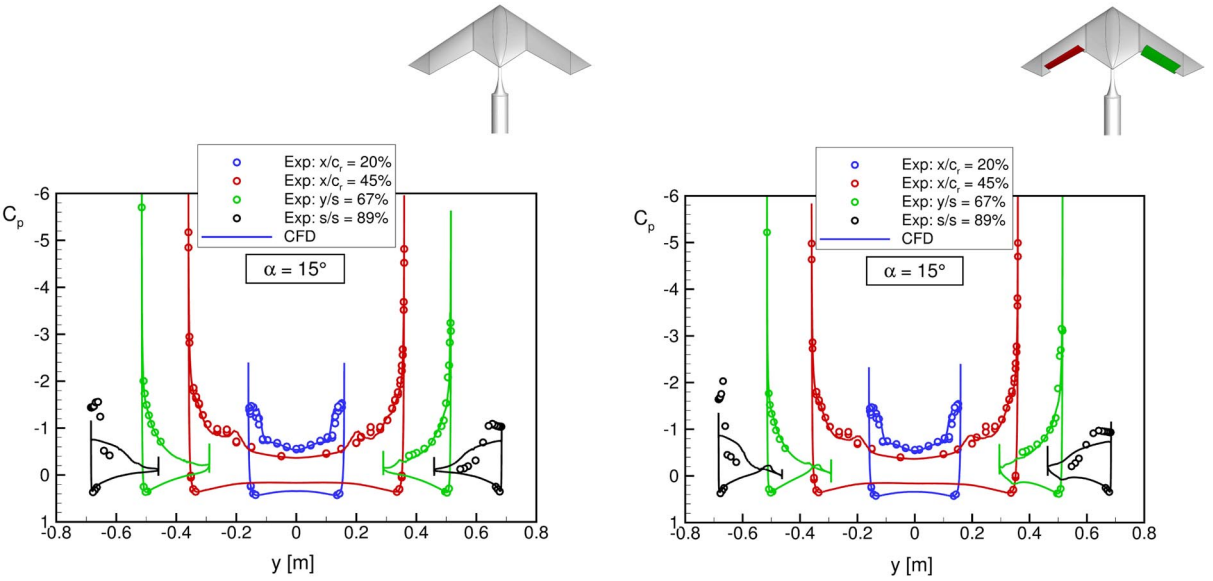

Fig. 28 BL and CS (LOBLIB/RIBROB) configuration: surface pressure distribution DLR TAU (RSM) vs experiment: $\alpha = 15$ deg.

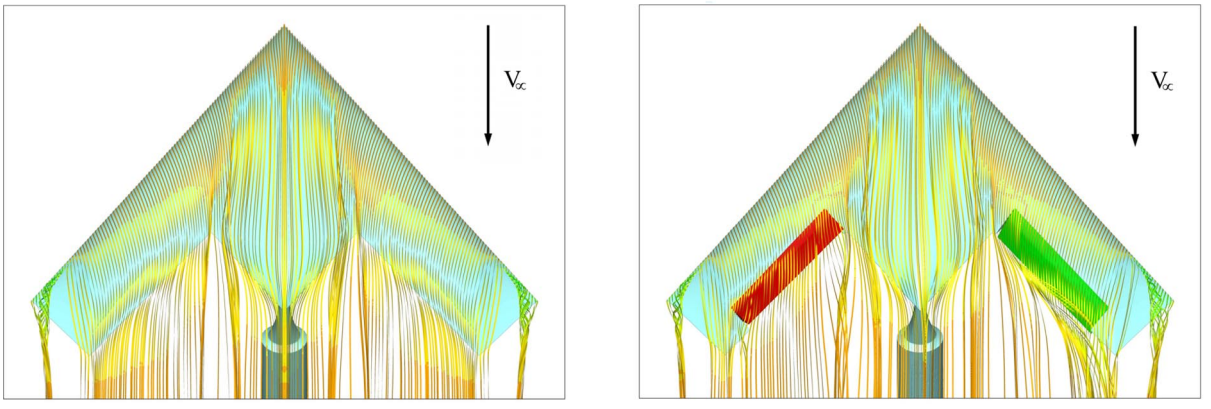

Fig. 29 Flow topology on the upper side of the DLR-F19 BL and LOBLIB/RIBROB configuration: $\alpha = 10$ deg, DLR TAU (RSM).

area, and thus a more rear loading pitching moment. With respect to the flow topology, this means that the tip vortices in Fig. 30 for $\alpha = 15$ deg are predicted too far upstream and an onset of vortex breakdown already occurs.

The flow over the control devices is significantly different between the two AOAs. For $\alpha = 10$ deg, the flow over the control devices is attached. The vortex from the apex is passing the control devices inboard. For $\alpha = 15$ deg, the apex vortex is bigger and is affecting the control devices inboard. The flow over the CS is dominated by vortical flow emanating from the former attached flow area between the apex and the tip vortex. The streamlines interacting with the CS are more or less parallel to the hinge line or trailing edge, respectively.

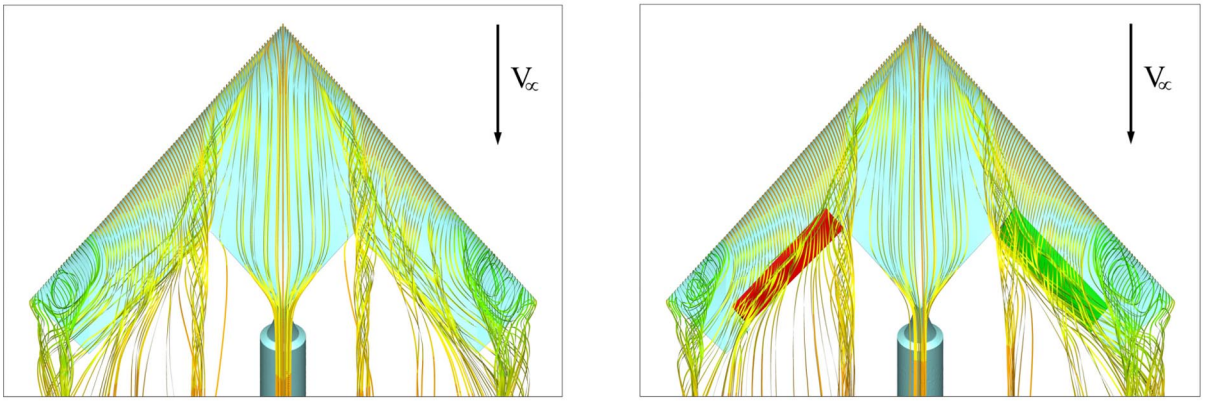

Fig. 30 Flow topology on the upper side of the DLR-F19 BL and LOBLIB/RIBROB configuration: $\alpha = 15$ deg, and DLR TAU (RSM).

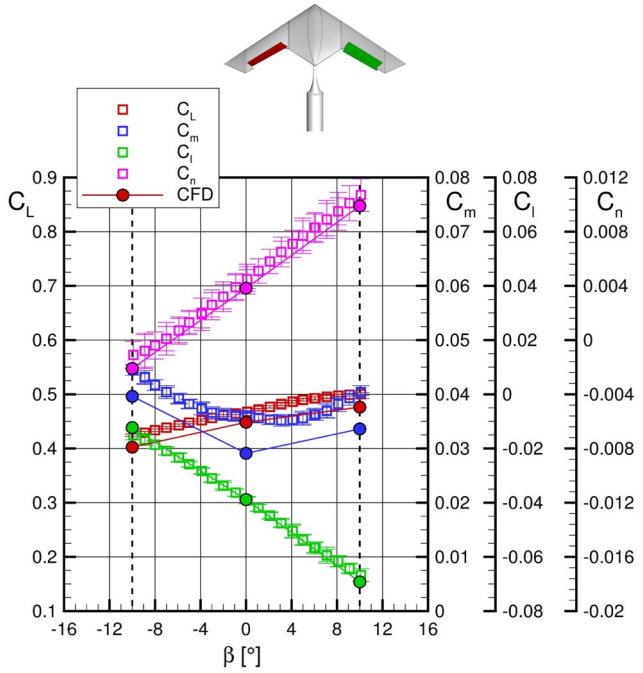

Fig. 31 DLR TAU (RSM) vs experiment: lift, pitching, rolling, and yawing moment coefficients, $\alpha = 10$ deg, $\beta = 10$ and -10 deg.

This reduces the dynamic pressure facing the CS, and thus the effectiveness of the control surfaces.

C. Asymmetric Onflow Conditions (DLR TAU Code)

In this section, the prediction capability and flow physics regarding asymmetric flow conditions will be discussed. Figure 31 shows, for the LOBLIB/RIBROB configuration, the lift, pitching, rolling, and yawing moment coefficients at an AOA of $\alpha = 10$ deg for three

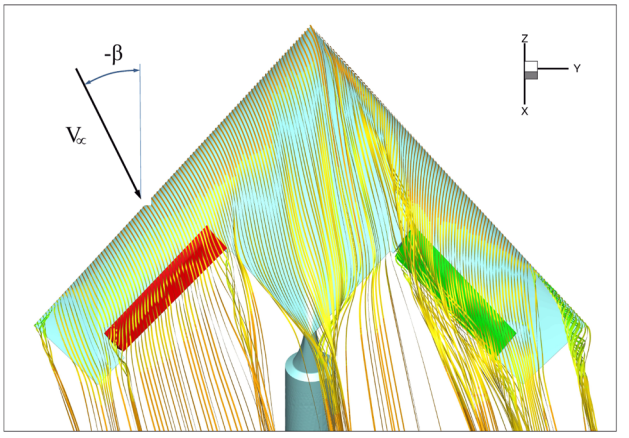

Fig. 33 Flow topology on the upper side of the DLR-F19 configuration: $\alpha = 10$ deg, $\beta = -10$ deg, and DLR TAU (RSM).

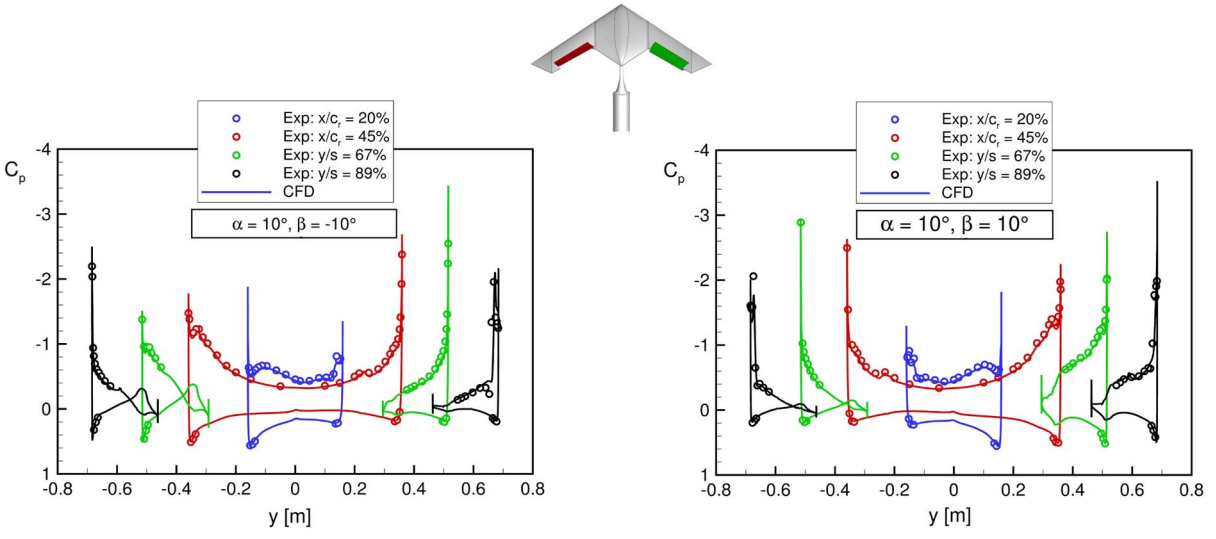

Fig. 32 CS (LOBLIB/RIBROB) configuration: surface pressure distribution DLR TAU (RSM) vs experiment: $\alpha = 10$ deg, $\beta = -10$ and 10 deg.

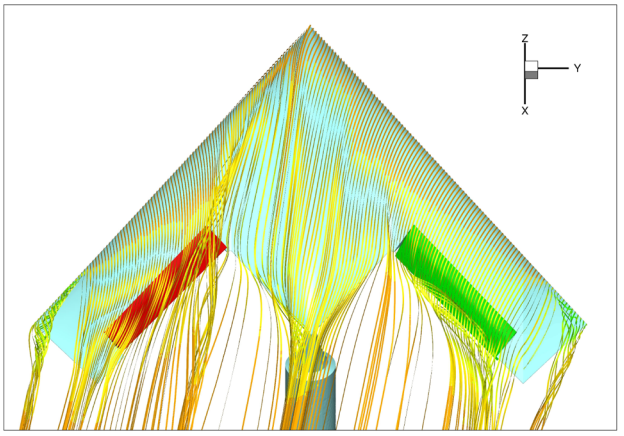

Fig. 34 Flow topology on the upper side of the DLR-F19 configuration: $\alpha = 10$ deg, $\beta = 10$ deg, and DLR TAU (RSM).

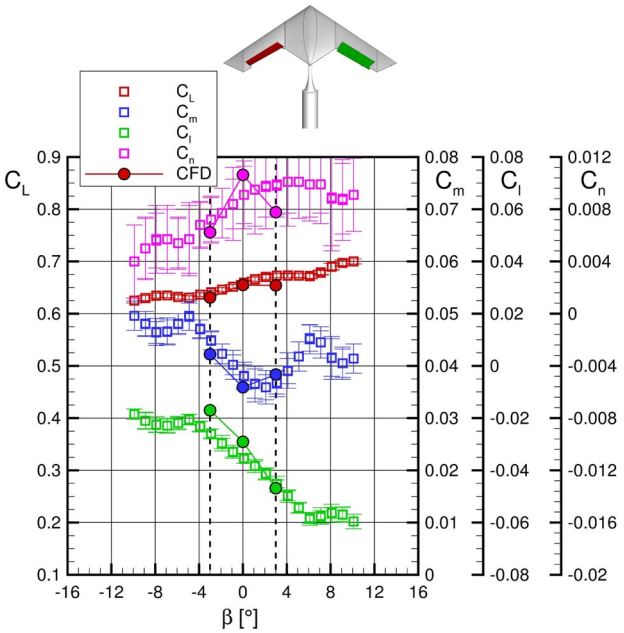

Fig. 35 DLR TAU (RSM) vs experiment: lift, pitching, rolling, and yawing moment coefficients: $\alpha = 14.7$ deg; $\beta = -3$ and 3 deg.

different angles of sideslip of $\beta = -10, 0$, and 10 deg in comparison to the experiment. It can be observed that the overall trend of the aerodynamic coefficients is predicted quite well by CFD in comparison to the experimental data. The pitching moment is underpredicted, which has already been observed in the results for the BL configuration. In Fig. 32, the surface pressure distribution is plotted for $\beta = -10$ and 10 deg. For both angles of sideslip (AOSs), the pressure distributions predicted by CFD match the experimental data very well.

Figures 33 and 34 show the flow topology for both $\beta = -10$ and 10 deg. In comparison to the symmetric flow conditions in Fig. 29, the apex vortex on the windward side of the wing has vanished due to the reduced, induced sweep angle. On the leeward side, the structure of the apex vortex is stronger than in the symmetric case. Comparing the two AOS cases with each other, there is not much difference in the pressure level, even though the flow on the leeward side for $\beta = -10$ deg gets accelerated by the downward flap deflection in opposition to the $\beta = 10$ deg case where the flow gets decelerated.

Overall, the CFD simulation represents the experiments very well with respect to the integral values and the pressure distribution.

Figure 35 shows the CFD results of the LOBLIB/RIBROB configuration in comparison to the experiment for an AOA of $\alpha = 14.7$ deg and AOSs of $\beta = -3, 0$, and 3 deg. As for the previous cases, the overall trend of the aerodynamic coefficients is predicted quite well by CFD in comparison to the experimental data. It can be seen that the rolling moment is slightly overestimated by the CFD simulations for $\beta = -3$ and 0 deg. The lift and pitching moment are predicted quite well in comparison to the experimental data. The magnitude of the yawing moment is very small and is considered irrelevant for this case.

Figure 36 shows the corresponding estimated pressure distributions in comparison to the experiment for $\beta = -3$ and 3 deg. For both AOSs, the pressure distribution is predicted in the front part correctly. The suction peaks of the tip vortex are on the left-hand side, and they are slightly underestimated for both AOSs.

Finally, in Fig. 37, the flow topology for the two AOSs is depicted. As already described in the previous example, the apex vortex on the leeward side of the wing is stronger than on the windward side. Although the AOS is quite small, the effect is relevant for the present AOA with respect to the roll stability. A positive sideslip causes a negative stabilizing rolling moment. The AOS is small enough that the apex vortex is not vanished on the windward side of the wing in comparison to the previous case at an AOS of $\beta = \pm 10$ deg.

In the previous figures, Figs. 31 and 35, the prediction capabilities have been discussed, comparing CFD simulations and taking the sting into account in comparison with the experiment. As discussed before, one uncertainty is the prediction of the flow around the sting support. The support influences the prediction accuracy of the integral aerodynamic coefficients. If the wake flow and resulting pressure distribution on the

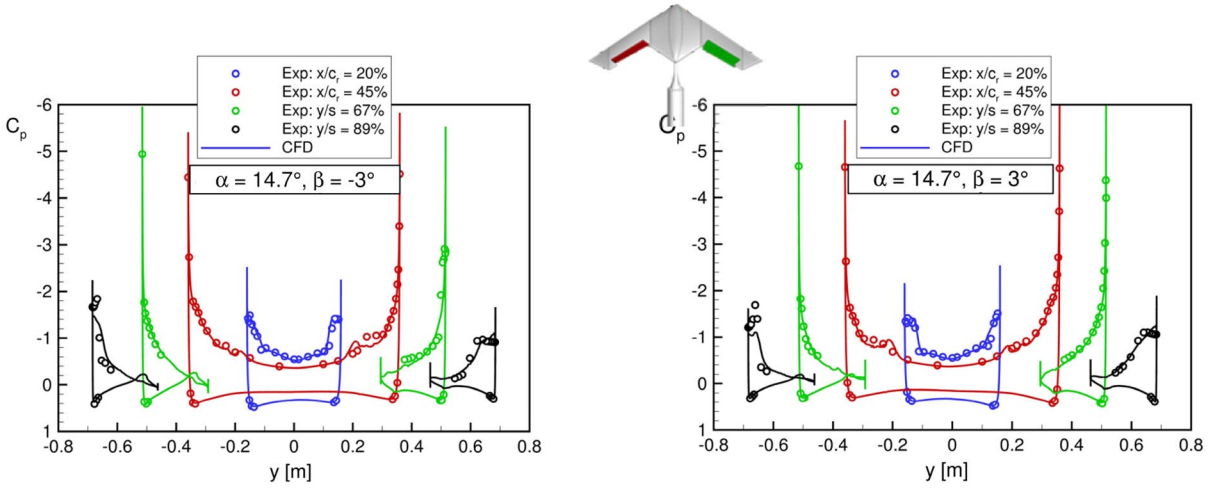

Fig. 36 CS (LOBLIB/RIBROB) configuration: surface pressure distribution DLR TAU (RSM) vs experiment: $\alpha = 14.7$ deg, $\beta = -3$ and 3 deg.

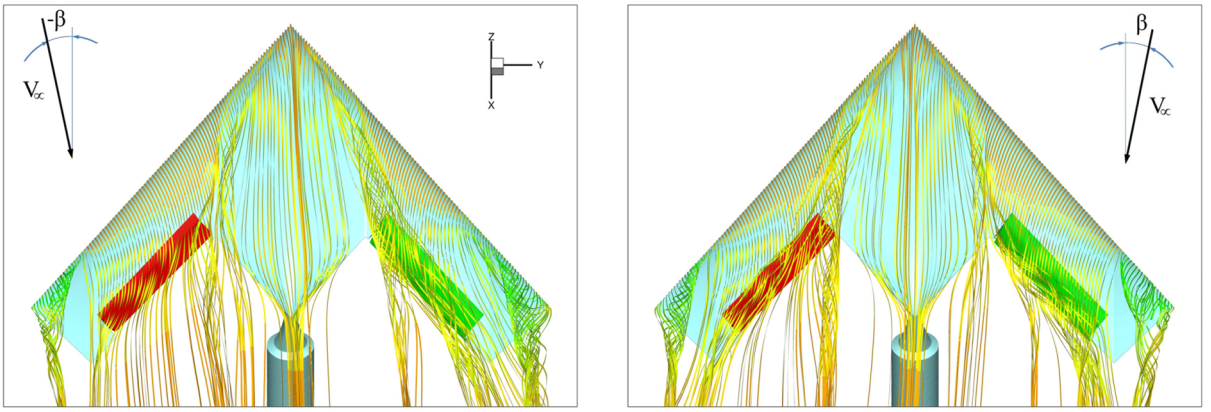

Fig. 37 Flow topology on the upper side of the DLR-F19 configuration: $\alpha = 14.7$ deg, $\beta = -3$ and 3 deg, and DLR TAU (RSM).

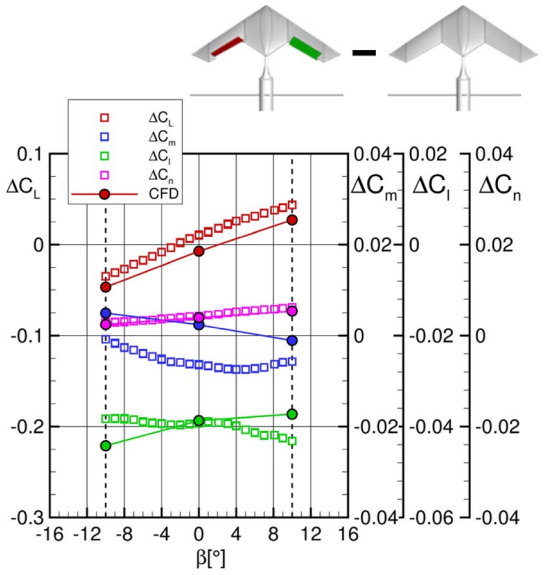

Fig. 38 DLR TAU (RSM) vs experiment: LOBLIB/RIBROB minus BL configurations at $\alpha = 10$ deg, $\beta = -10$ and 10 deg (with sting support).

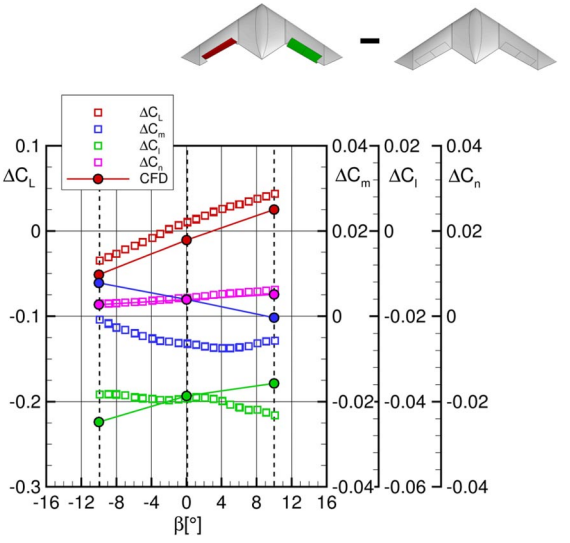

Fig. 40 DLR TAU (RSM) vs experiment: LOBLIB/RIBROB minus BL configurations at $\alpha = 10$ deg, $\beta = -10$ and 10 deg (no sting support).

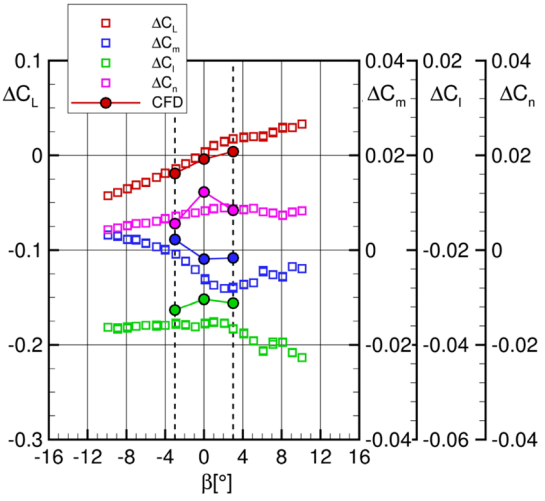

Fig. 39 DLR TAU (RSM) vs experiment: LOBLIB/RIBROB minus BL configurations at $\alpha = 14.7$ deg, $\beta = -3$ and 3 deg (with sting support).

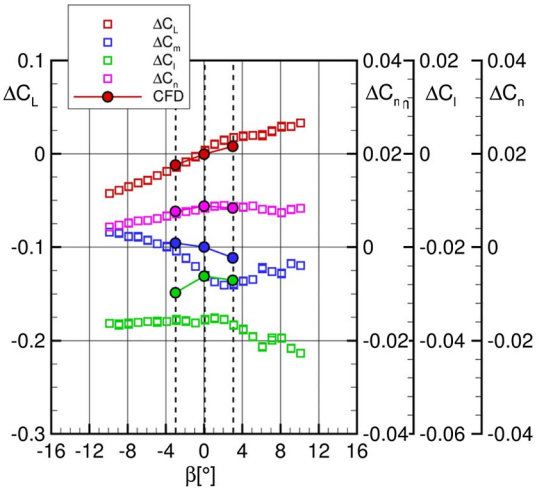

Fig. 41 DLR TAU (RSM) vs experiment: LOBLIB/RIBROB minus BL configurations at $\alpha = 14.7$ deg, $\beta = -3$ and 3 deg (no sting support).

Table 6 Static α/β sweeps; SACCON DLR-F19

DLR TN2545 [20]	LOB/LIB, deg	ROB/RIB, deg	α, deg	β, deg	M_∞	Re_{cref}, million
1001	— —	— —	0–30	0	0.146	1.57
1103	−20/ − 20	+20/ + 20	0–30	0	0.146	1.57
1007	— —	— —	10.48	+10, . . . , −10	0.146	1.57
1109	−20/ − 20	+20/ + 20	10.48	+10, . . . , −10	0.134	1.46
1008	— —	— —	14.67	+10, . . . , −10	0.146	1.57
1110	−20/ − 20	+20/ + 20	14.67	+10, . . . , −10	0.134	1.46

lower side of the wing is not predicted correctly, it might have significant influence on the prediction of the pitching moment.

In Figs. 38 and 39, the differences of the stability and control values between the configuration with and without control device deflection are plotted against each other. It can be observed that the values of the differences in lift, pitching, and yawing moments can be predicted reasonably accurately. The differences in the rolling moment are in a similar range; although, for the case at $\alpha = 10$ deg and $\beta = \pm 3$ deg, the trend is not represented correctly.

In Figs. 40 and 41, the same values are plotted as in Figs. 38 and 39, with the difference that, now, the sting support is not taken into account in the CFD simulations. The idea was that using CFD simulations without the sting might enhance the match between CFD and the experiment. Hence, it would reduce the computational effort by not including the sting support. Looking at the plot in Fig. 40 for $\alpha = 10$ deg and $\beta = \pm 10$ deg, almost no difference appears between both approaches. The differences in the lift, rolling, and yawing moments are the same as in Fig. 38. The pitching moment

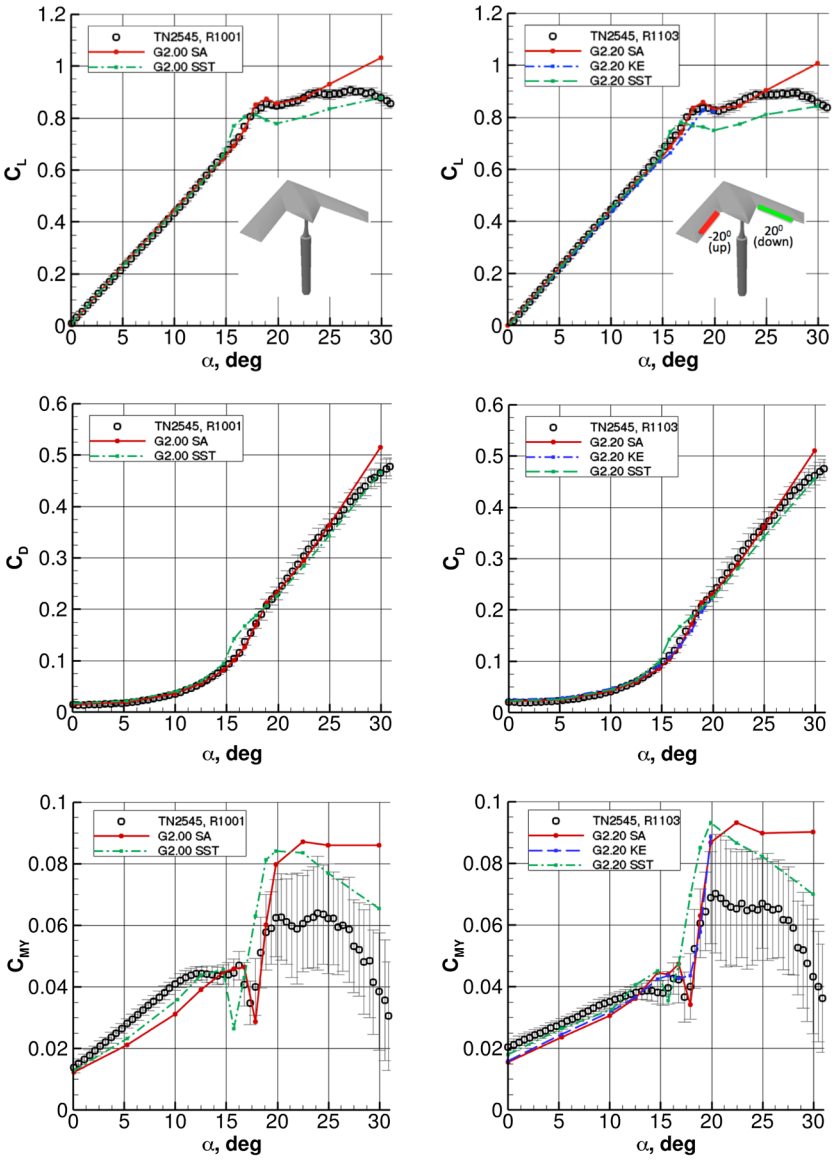

Fig. 42 Effect of turbulence models for static coefficients. CS0 (left) and CS20 (right) $M_\infty = 0.14$, $Re_{\text{cref}} = 1.40$ million. NASA USM3D, grid 2.

differences are slightly higher in the case without the sting in Fig. 40. Similar differences apply for the case in Fig. 41 for $\alpha = 14.7$ deg, $\beta = -3$ and 3 deg and Fig. 39, respectively. For this case, the differences in the CFD simulations in the rolling moment are higher than for the case where no sting support is taken into account.

It seems to be that the sting support has slightly more influence on the overall flow physics than just on the flow around the lower rear part of the configuration. Hence, the differentials are not just neglecting the sting effect.

D. Symmetric and Asymmetric Onflow Conditions (NASA USM3D)

Correlations of computational and experimental results are presented to assess CFD predictive capabilities for the static of the SACCON configuration with and without control surface deflections. A cursory α sweep is generated with the DLR-F19 to provide overlap with prior SACCON computational results provided by Frink [50] and to assess the longitudinal aerodynamics of the configuration with deflected control surfaces. Then, a series of β sweeps is performed to assess grid and turbulence model sensitivities, as well as to investigate static lateral/directional Stability and control characteristics.

As depicted in Table 6, the static investigation includes two angle-of-attack sweeps for $\alpha = 0 - 30$ deg: one with and one without control surface deflection. Solutions are provided at $\alpha = 0.0$, 5.3, 10.0, 12.5, 14.7, 15.7, 16.8, 17.8, 18.9, 19.9, 22.5, 25.0, and 30.0 deg, as well as zero sideslip. Static sideslip sweeps of $\beta = \pm 10$ deg at $\Delta\beta = 1$ deg increments are performed at $\alpha = 10.48$ and 14.67 deg. The corresponding correlation dataset from the DLR's wind-tunnel test [20] is listed in the first column. All cases will be computed on the G1, G2, and G3 grids from Table 3. The SA, Mentor sheer stress transport, and Jones–Launder linear k-ε two-equation turbulence model (KE) turbulence models will be assessed on select grids.

1. α Sweep

A series of static time-accurate USM3D flow solutions were generated on the DLR-F19 for 13 angles of attack between 0 and 30 deg to explore the sensitivity of the turbulence model on the medium grids G2.00 and G2.20 (see Tables 3 and 6). The SA and SST

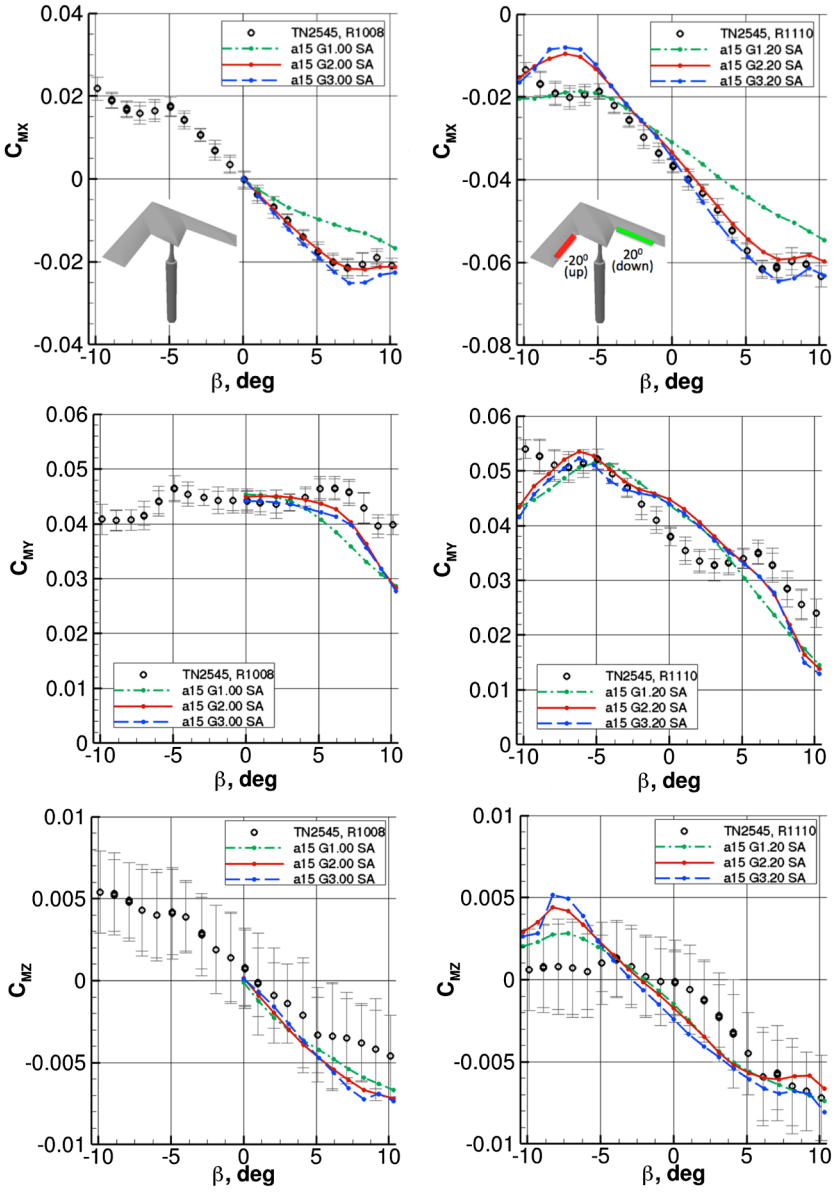

Fig. 43 Effect of grid refinement for static lateral/directional moment coefficients. CS0 (left) and CS20 (right). $M_\infty = 0.14$, $Re_{cref} = 1.40$ million, $\Theta_0 = 14.67$ deg. NASA USM3D/SA.

turbulence models were applied to both grids, and the k-ε model was only applied to the G2.20 that has a 20-deg. control surface deflection (CS20).

The non-deflected control surface cases (CS0) used a prescribed characteristic time step of $\Delta t^* = 0.02$, where physical $\Delta t = \Delta t^* \times c_{\text{ref}}/V_\infty$. Solutions were advanced in time for 2000 time steps, allowing the flow residual of the inner iterations to drop 2.5 orders of magnitude, which typically require five to six inner iterations of the second-order physical time-step scheme. This approach provided a total of 40 characteristic time steps for solution convergence, which was verified. The CS20 cases required a more aggressive strategy due to the additional complexity of asymmetric control surface deflection. Hence, a characteristic time step of $\Delta t^* = 0.10$ was prescribed for 2000 time steps, increasing the total number of characteristic time steps to 200. Some test solutions were run on the CS0 case to confirm that the change in Δt^* had negligible impact on the converged solution, which was expected due to the strong flow damping from Reynolds averaging.

Comparisons of the lift, drag, and pitching moment coefficient variations with the angle of attack are presented in Fig. 42 for both CS0 (left) and CS20 (right) configurations. The flow physics behind the behavior of the experimental data [20] with increasing angle of attack α is well documented [16] and will not be repeated. The correlations of the USM3D SA and SST turbulence model results for the undeflected CS0 case are similar to those published during the AVT-161 study [17]. In general, both the SA and SST models correlate well for C_L and C_D in the linear range up to $\alpha \approx 15$ deg.

The C_{MY} is underpredicted in the linear range, which is typical of all RANS correlations from the AVT-161 task group. A stronger sensitivity is observed at the higher poststall angles. Note the large uncertainty bands on C_{MY} for the experimental data above $\alpha > 17$ deg, which infer highly unsteady flow. The poor correlations of CFD in this range suggest that the inherent dissipation of the RANS formulation caused by excessive levels of viscosity damps any critical unsteady flow features that would influence this sensitive region of the angle-of-attack range. The SST model does yield a better correlation of poststall due to its known quality of producing lower levels of turbulent viscosity than SA for highly separated flows.

The deflected CS20 correlations on the right side of Fig. 42 reflect the general character of the CS0 case. However, in addition to the SA

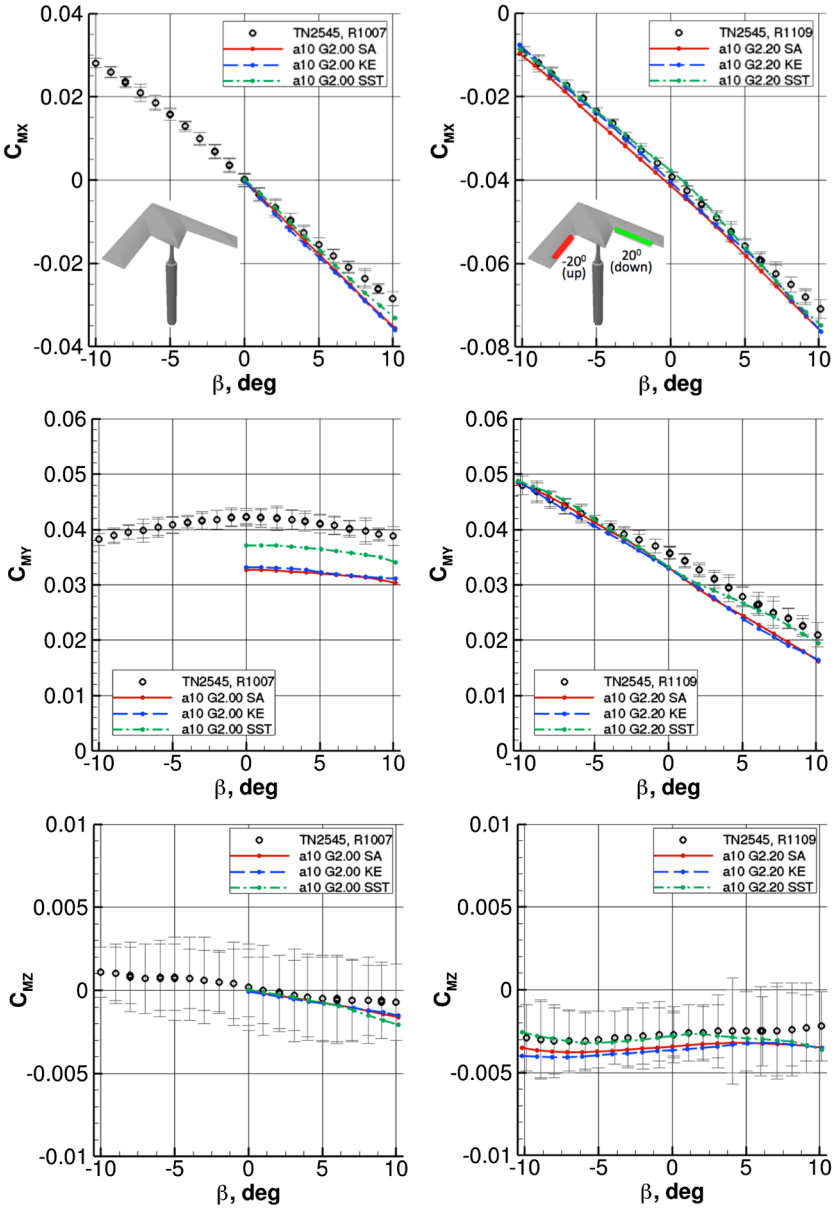

Fig. 44 Effect of turbulence model: static lateral moment coefficients. CS0 (left) and CS20 (right). $M_\infty = 0.14$, $Re_{c\text{ref}} = 1.40$ million, $\Theta_0 = 10.48$ deg. NASA USM3D, grid 2.

and SST models, the KE model has been added. The KE model offers no significant improvement to the correlations with experimental data. Furthermore, this model failed to run beyond $\alpha = 20$ deg, thereby preventing any assessment in the poststall region.

2. *β Sweeps*

A series of static sideslip sweeps (Table 6) were generated on the DLR-F19 to explore the sensitivity of grids (Table 3) and turbulence models. The SA, SST, and KE turbulence models were applied to both CS0 and CS20 grids.

A physical time step of $\Delta t = 0.00167$ s was prescribed for the sideslip sweeps, which result in a characteristic time step of $\Delta t^* = 0.165$. A total of 25 inner iterations were performed between each time step. The sweeps were computed with one continuous run using the prescribed motion capability from FD-CADRE. Restarting from a converged zero-sideslip initial solution at the angle of attack, the configuration was moved in 1 deg increments of sideslip over 10 time steps and then held on point for 290 time steps ($\Delta t^* \approx 48$) before moving to the next point. Convergence to steady state was confirmed within each increment. The advantages of this strategy are that it 1) requires a factor of 3.5 less computer time than a comparable set of individual runs; and 2) mimics the wind-tunnel test technique, which could potentially have path dependencies that affect the progression of leading-edge flow separation with increasing sideslip.

The selection of the baseline grids for CS0 and CS20 is determined from the results in Fig. 43, which convey the variations of static roll, pitch, and yaw moments (C_{MX}, C_{MY}, and C_{MZ}), with β at the more challenging pitch angle of $\Theta_0 = 14.67$ deg. The experimental data [20] are plotted with symbols and uncertainty bounds. Note that the moments for the CS0 case on the left side are relatively symmetric, whereas those for CS20 with asymmetric control deflections are less so. Solutions were computed with USM3D/SA on grids G1, G2, and G3 from Table 3. For the symmetric CS0 cases, solutions were only computed in the positive β-sweep direction (nose left). It is immediately obvious that G1 is not adequate for either the CS0 or CS20 case. Grids G2 and G3 generally capture the slope of the moments (i.e., static stability) and, to a lesser extent, the inflection in C_{MX} and C_{MZ} at $\beta \approx \pm 5$ deg caused by a sudden change in flow state. It is also encouraging that grids G2 and G3 also produce the correct offset in negative rolling moment $C_{MX} \approx -0.035$ at $\beta = 0$ deg for CS20. Differences are observed in the offset and character of C_{MZ} for CS20, but most of the USM3D/SA solutions fall within the uncertainty range of the

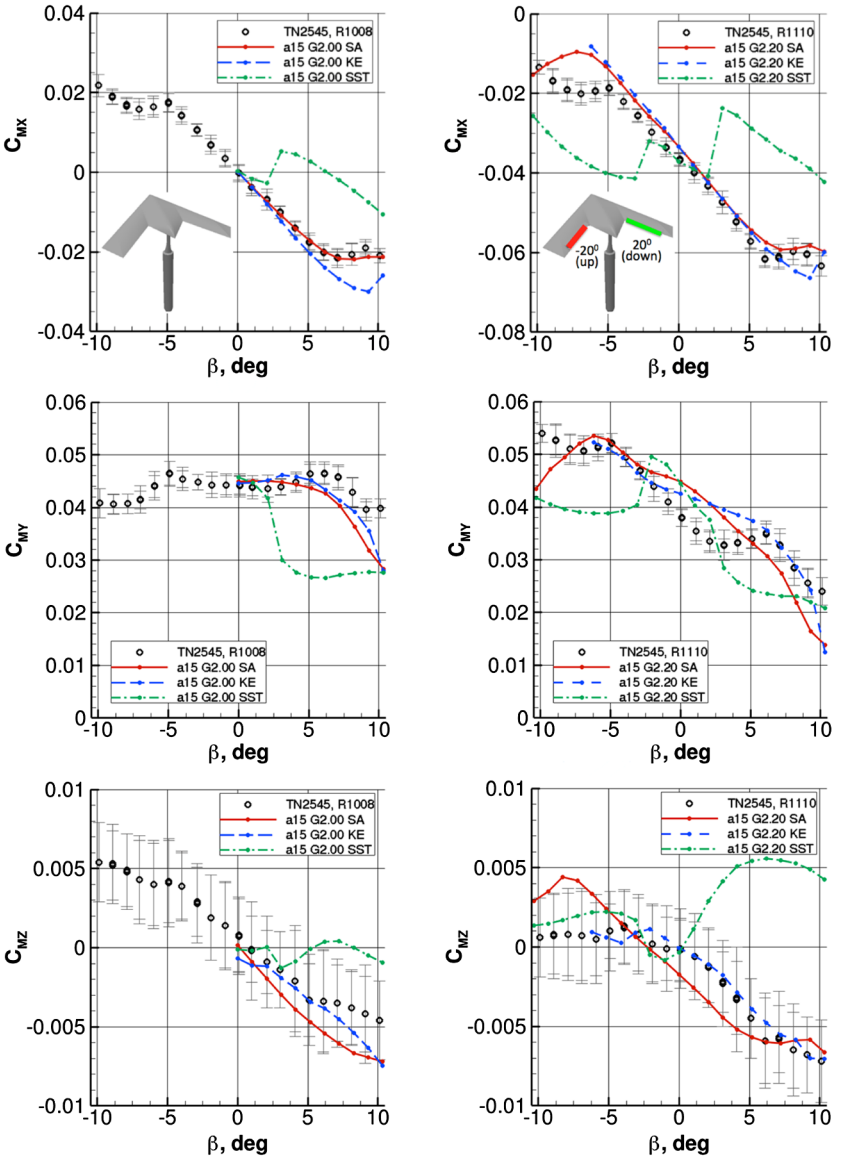

Fig. 45 Effect of turbulence model: static lateral moment coefficients. CS0 (left) and CS20 (right). $M_\infty = 0.14$, $Re_{cref} = 1.40$ million, $\Theta_0 = 14.67$ deg. NASA USM3D, grid 2.

data for C_{MX} and C_{MZ}. Considering the increasingly large cell count of grids G2 and G3, and their reasonably close correlation of results between these two grids in Fig. 43, the G2.00 (13 million cells) and G2.20 (18 million cells) grids will be selected for further assessment of turbulence models.

Figure 44 shows the effect of the SA, KE, and SST turbulence models on the static lateral/directional moment coefficients at the lower pitch angle of $\Theta_0 = 10.48$ deg using the medium grids G2. Again, the CS0 is on the left and CS20 on the right. The experimental data, plotted with symbols and uncertainty bounds, exhibit a well-behaved almost linear quality. The USM3D solution results from the three turbulence models also correlate reasonably well with the experiment. However, the SST model renders the best overall correlation.

A similar correlation of turbulence models for the higher pitch angle of $\Theta_0 = 14.67$ deg in Fig. 45 yields a more surprising result. The SST model degenerates dramatically for both CS0 and CS20 beyond β of ± 2 deg, whereas the SA and KE models retain reasonable correlations. The reason for this departure is evident in the corresponding surface C_p contours and streamlines presented in Fig. 46 for $\beta = +5$ deg. At this sideslip, the rolling moment C_{MX} in Fig. 45 for the SST solution on the CS0 case shows a sudden departure in the positive direction away from the experimental data and the SA/KE solutions. Similarly, the yawing moment C_{MZ} for the CS20 solution with the SST model in Fig. 45 exhibits a similar sudden departure in the positive direction that extends well outside of the experimental uncertainty bounds.

In Fig. 46, the SA and KE models produce a partially attached flow with accompanying low pressure along a majority of the right (windward) wing leading edge, as well as the beginnings of a leading-edge vortex near the left wingtip. This is consistent with the production of a negative rolling moment C_{MX}. The SST model results in Fig. 46 reveal a well-developed leading-edge vortex and accompanying low pressure on the left wing, as well as a more stalled flow with increasing pressures on the right wing, which is consistent with the production of a positive rolling moment C_{MX}. Numerous attempts were made to resolve the problem with the SST model [e.g., running of the finer G3 grids (Table 3), decrease of the time step Δt,

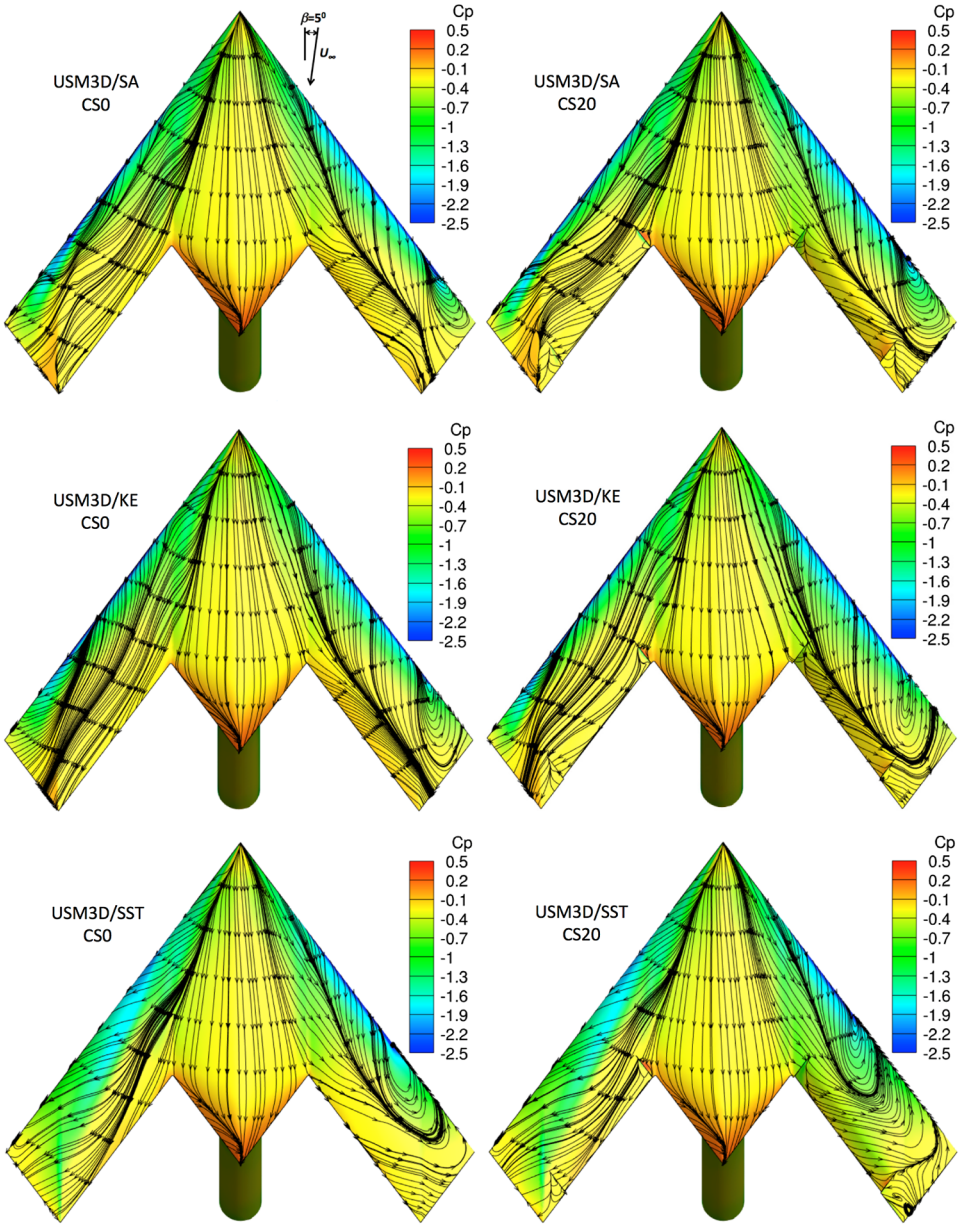

Fig. 46 Effect of turbulence model: surface C_p contours and streamlines at $\beta = 5$ deg. CS0 (left) and CS20 (right). $M_\infty = 0.14$, $Re_{\text{cref}} = 1.40$ million, $\Theta_0 = 14.67$ deg. NASA USM3D, grid 2.

increase of the number of inner iterations, decrease of the rate of incremental sideslip motion, an initialized solution from the freestream condition, etc.], but nothing produced a significantly different result. In past experiences, the SST model has been a very reliable model of choice for many complex applications. However, it appears that the SACCON configuration at this higher angle-of-attack sideslip condition has exposed a shortcoming in the turbulence model.

Overall in Fig. 45, the KE model yields the best correlations with the experimental data. Unfortunately, KE solutions could not be obtained for $\beta < -6$ deg. Hence, this model lacks the robustness for general use on the SACCON. For these reasons, the SA model is selected as the preferred model for this application.

E. Dynamic Simulations (DLR TAU Code)

Forced Oscillation in Pitch. In this section, the dynamic aerodynamic behavior will be discussed. The pitching motion of the BL and LOBLIB/RIBROB configuration in comparison to the experiment will be taken as an example to evaluate the dynamic prediction capability for low- and medium-range AOAs. For both simulations, the motion frequency is 2 Hz and the model is pitching around an AOA of $\theta_0 = 10$ deg with an amplitude of $\Delta\theta = 5$ deg. The model is pitching around an axis at 84% root chord that is 24% behind the MRP. The physical time-step size has been $\Delta t = 0.001$ s ($\Delta t^* = 0.104$), which leads to 500 physical time steps simulated within one time period.

In Fig. 47, the numerical results in comparison to the experiment are shown for $\theta = 14$ deg with increasing and decreasing AOA motion. On the left-hand side, the CFD simulated pressure distributions are plotted in comparison to the experiment. For both upward and downward types of motion, no significant difference can be observed. The comparison of the curves between the simulation and the experiment shows no difference in the normal force coefficient. But, large differences are observed with the pitching moment coefficient. The normal force shows no hysteresis effects, and both curve gradients are the same. The pitching moment, on the other hand, shows a hysteresis where both the shape and gradient of the hysteresis curve are different between the CFD simulation and the experiment. Nevertheless, the deltas in absolute values for both types of motion on the hysteresis for $\theta = 14$ deg are comparable to the deltas that have been observed in the steady-state simulations.

On the right-hand side, the simulated streamlines for both motions on the hysteresis for $\theta = 14$ deg are depicted. It can be observed that the topology of the vortex structure over the wing is the same but, for the downward motion, the apex vortex tends to be stronger and the tip vortex weaker due to the onset of vortex breakdown. This slight

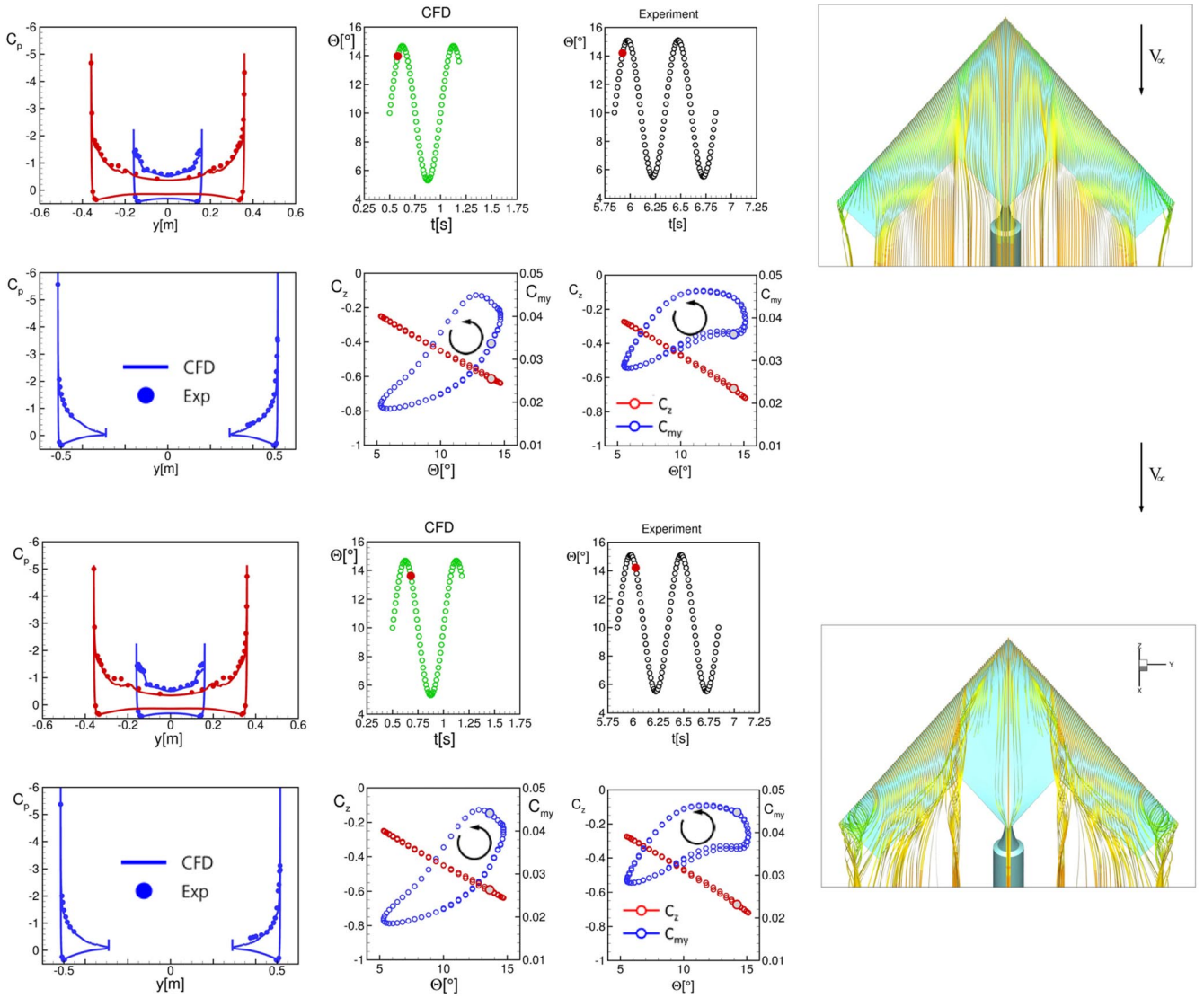

Fig. 47 Pitching motion (BL configuration): $\Theta_0 = 10$ deg, $\Delta\theta = 5$ deg, $f = 2$ Hz; DLR TAU (RSM) vs experiment. Upward motion top; downward motion bottom.

difference can also be observed for the apex vortex comparing the pressure distribution for upward and downward motions. This causes a more positive rear loading pitching moment for the downward motion than for the upward one. The difference is small, but the pitching moment is very sensitive due to the position of the MRP, as discussed before.

In Fig. 48, the results for $\theta = 10$ deg for the upward and downward motions are depicted. For $\theta = 10$ deg, the same effect occur as previously discussed for $\theta = 14$ deg.

Overall, it can be observed that the dynamic pressure distribution over the wing and the trajectory of the normal force can be predicted quite well by the numerical simulation. However, the shape and gradient of the pitching moment hysteresis is predicted differently, but the incremental differences at various pitch angles are comparable to the differences observed for the steady-state solutions.

Figure 49 shows the results of the corresponding pitching maneuver of the LOBLIB/RIBROB configuration. As an example, the case for an AOA of $\theta = 10$ deg should be discussed for the upward and downward motions. As for the BL configuration, the simulated surface pressure distribution matches the experimental data very well.

With respect to the normal force, it can be observed that there is again no difference between the CFD simulations in comparison to the experiment in the same way as for the BL configuration. For the pitching moment, there is a significant hysteresis loop that matches much better with the experimental data for the present CS case than before for the BL configuration. This applies for the thickness of the loop and for the gradient.

On the right-hand side of Fig. 49, the flow topology on the upper side of the wing is depicted. For the upward motion at $\theta = 10$ deg, we have again more or less fully attached flow with a small apex vortex and a small vortical flow separation at the wingtips. For the downward motion, the apex vortex is much stronger than the tip vortices in comparison to the upward motion as well. In comparison to the BL configuration, the location of the apex vortex on the left-hand side is slightly more inboard, and the one on the right-hand side is slightly more outboard due to the control surface deflections.

Both test cases without and with control surface deflection show a reasonable match of the dynamic behavior in comparison to the experimental data. There is a difference in the shape of the hysteresis loop of the pitching moment for both configurations, as well as in the gradient of the loop for the BL configuration. Both pitching moment curves show significant nonlinearities, which have been already discussed regarding the steady-state solution. An assessment of how relevant these differences are for stability and control estimations has

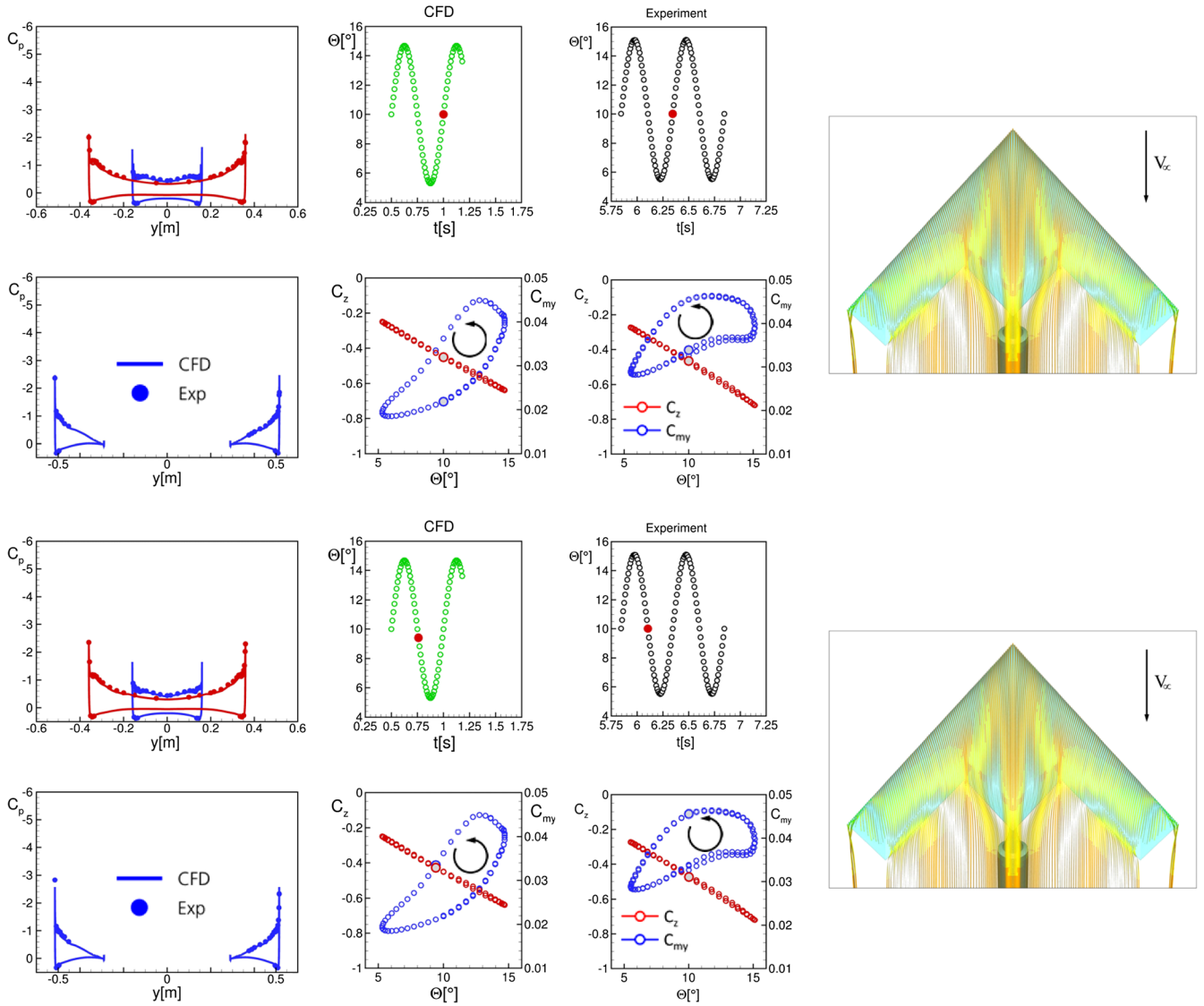

Fig. 48 Pitching motion (BL configuration): $\Theta_0 = 10$ deg, $\Delta\theta = 5$ deg, $f = 2$ Hz; DLR TAU (RSM) vs experiment. Upward motion top; downward motion bottom.

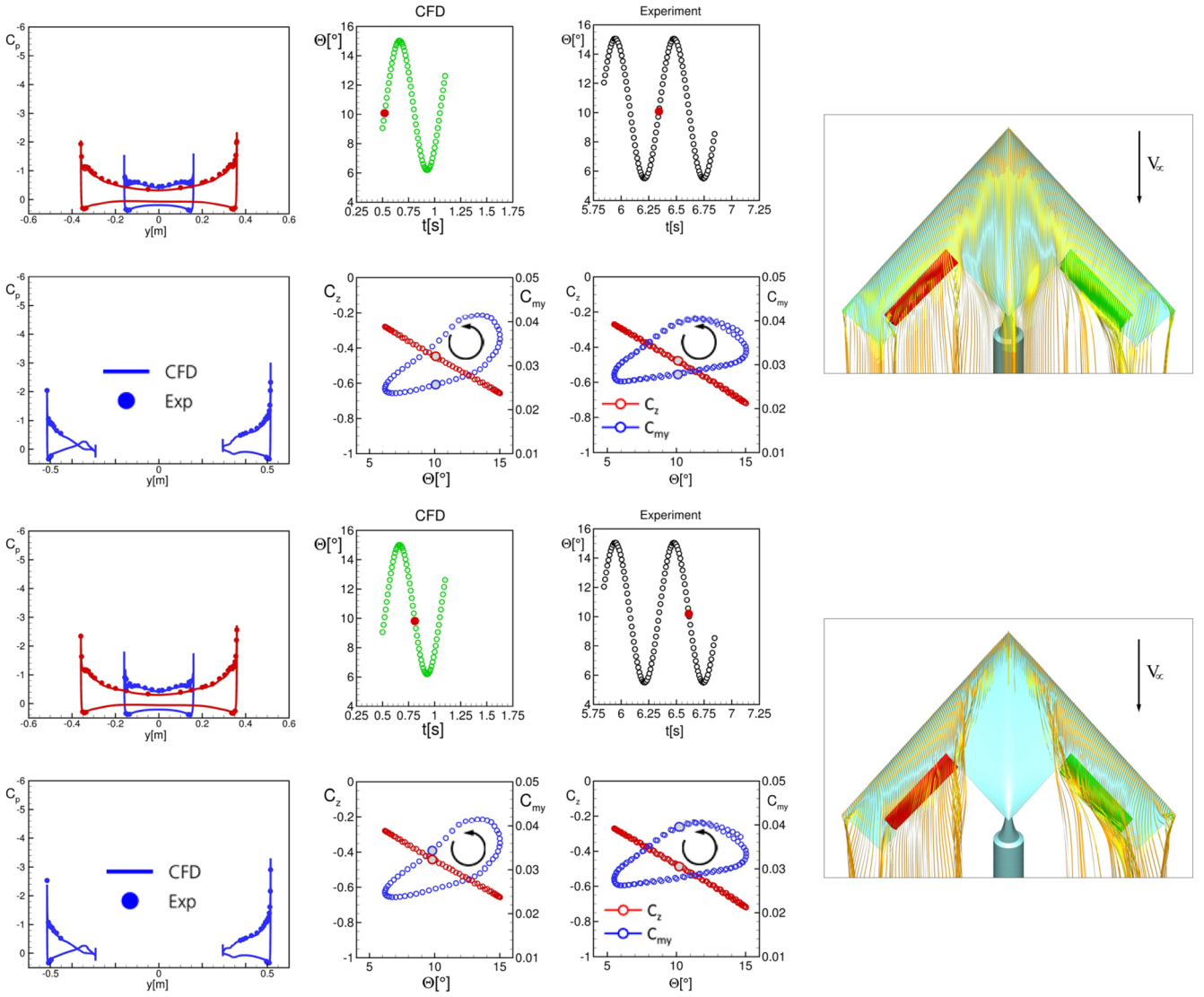

Fig. 49 Pitching motion (LOBLIB/RIBROB configuration): $\Theta_0 = 10$ deg, $\Delta\theta = 5$ deg, $f = 2$ Hz; DLR TAU (RSM) vs experiment. Upward motion top; downward motion bottom.

to be done by substituting experimental data for the CFD datasets in the flight mechanics model. The differences from comparing the system answer of the experimental-based flight mechanics model with that from the CFD-based model are expected to be small in the linear regime. In the nonlinear regime, this might be not the case regarding the results presented in this paper. The assessment of the differences in the nonlinear regime is acceptable for stability and control predictions and will be evaluated in a task group in the near future.

F. Dynamic Simulations (NASA USM3D)

Correlations of dynamic stability and control characteristics are presented with forced sinusoidal motion imposed about the pitch, yaw, and roll axes. The pitch and yaw oscillations are imposed at the point of rotation POR$[x, y, z] = [0.855, 0, 0]$ m location, and the moments are transferred to the MRP. The support stings are not included in the force and moment integrations. As a reminder, the cases with undeflected control surfaces will be designated as CS0, and the cases with deflected control surfaces of LOB/LIB $= -20/-20$ deg and ROB/RIB $= +20/+20$ deg will be designated as CS20. All moment coefficients are presented in the body axis system and are designated as C_{MX}, C_{MY}, and C_{MZ} for the roll, pitch, and yaw, respectively.

Sinusoidal oscillations about the pitch and yaw axes were imposed on the DLR-F19 SACCON at POR$[x, y, z] = [0.855, 0, 0]$ m through the FD-CADRE trajectory input file. The roll oscillations for the DLR-F17 were prescribed by an internal motion generator within USM3D. The forced oscillation computations were initiated by solution restart from converged time-accurate static solutions at the nominal pitch angle $\Theta_0(\alpha_0)$, roll angle of $\Phi_0 = 0$ deg, and yaw angle of $\Psi_0 = 0$ deg. Although the dynamic force and moment coefficients were essentially converged to their periodic solution after the first quarter-oscillation cycle, the solutions were continued for two full sinusoidal cycles in this study. The second cycle was used for comparisons to eliminate any transients from the plots. The time-accurate RANS solution exhibited a deterministic quality by converging to a very stable solution, in contrast to the well-known unsteadiness in the experimental data. The support sting moved with the wing in solid body motion, but it was not included in the force and moment integrations. The moments are transferred from the POR to the MRP.

The USM3D convergence guidelines for dynamic RANS simulations were developed by Frink [50]. In general, a well-converged solution is insured using a total of 36,000 iterations per oscillation cycle, regardless of the combination of outer time steps and inner iterations. This guideline is overly conservative for many

Table 7 Common dynamic test cases for pitch F-O. SACCON DLR-F19, $\Phi_0 = 0$ deg, and $\Psi_0 = 0$ deg

DLR TN2545 [21]	LOB/LIB, deg	ROB/RIB, deg	Θ_0, deg	$\Delta\Theta$, deg	f, Hz	$k_P\ 2\pi f \cdot c_{\text{ref}}/U_\infty$	M_∞	Re_{cref}, million
2342-50	— —	— —	10.3	4.7	1	0.06	0.146	1.57
2351-59	— —	— —	10.3	4.7	2	0.12	0.146	1.57
2666-74	−20/ − 20	+20/ + 20	10.3	4.7	0.94	0.06	0.138	1.49
2675-83	−20/ − 20	+20/ + 20	10.3	4.7	1.88	0.12	0.138	1.49

conditions, but it does insure convergence of the more difficult nonlinear cases using a single strategy.

A physical time step of $\Delta t = 0.00167$ s was selected for the current computations to match that in the experimental data. For CS0 cases with oscillation frequencies of 1.00 and 2.00 Hz, this results in $\Delta t^* = 0.174$ and respective time steps per cycle of 600 and 300 with corresponding inner iterations of 60 and 120 to maintain a total of 36,000 total iterations per cycle. Similarly for CS20 cases with oscillation frequencies of 0.94 and 1.88 Hz, $\Delta t^* = 0.165$ with respective time steps per cycle of 638 and 320 with corresponding inner iterations of 56 and 113.

1. *Forced Oscillation in Pitch (NASA USM3D)*

The AVT-201 common test cases for forced oscillation in pitch are listed in Table 7. Two reduced frequencies for sinusoidal pitch oscillations are assessed about a nominal pitch angle, with and without control surface deflections. The corresponding correlation dataset from the DLR's wind-tunnel test [21] is listed in the first column. The Mach and Reynolds numbers are adjusted in the computations to correspond with their respective test conditions. The appropriate grids were selected from the results of the static study.

The cases for pitch oscillation of the DLR-F19 are listed in Table 7. Low- and high frequency oscillations of $\Delta\Theta = \pm 4.7$ deg about an initial pitch angle of $\Theta_0 = 10.3$ deg are investigated for $k_P = 2\pi f \cdot c_{\text{ref}}/U_\infty$ of 0.06 and 0.12. These reduced frequencies correspond, respectively, to 1.00 and 2.00 Hz for CS0, and 0.94 and 1.88 Hz for CS20 cases.

An important inconsistency in configuration is noted; the experimental pitch oscillations from work by Vicroy et al. [21] were imposed using a pitch link support with a 6 deg crank angle and an axis push rod. Hence, there was relative motion between the

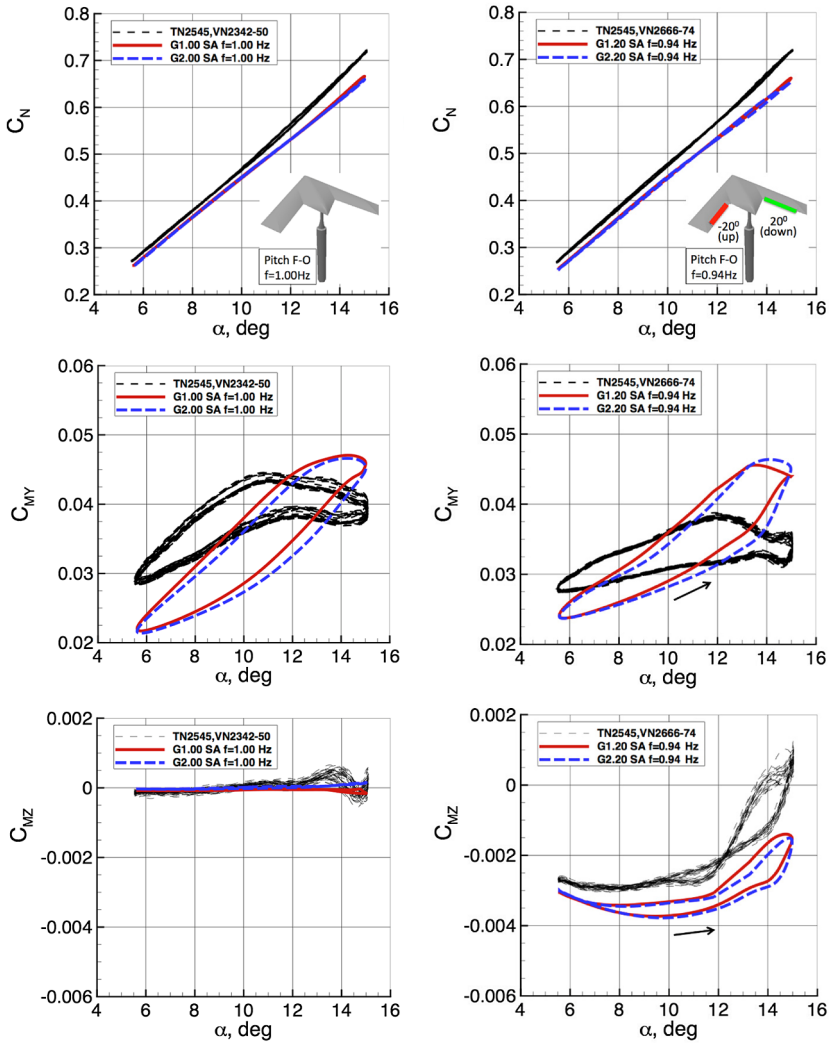

Fig. 50 Effect of grid density under low-frequency pitch oscillation ($k_P = 0.06$), $\Theta_0 = 10.3$ deg, and $\Delta\Theta = \pm 4.7$ deg. CS0 (left) and CS20 (right). $M_\infty = 0.14$, $Re_{\text{cref}} = 1.5$ million. NASA USM3D/SA, grids 1 and 2.

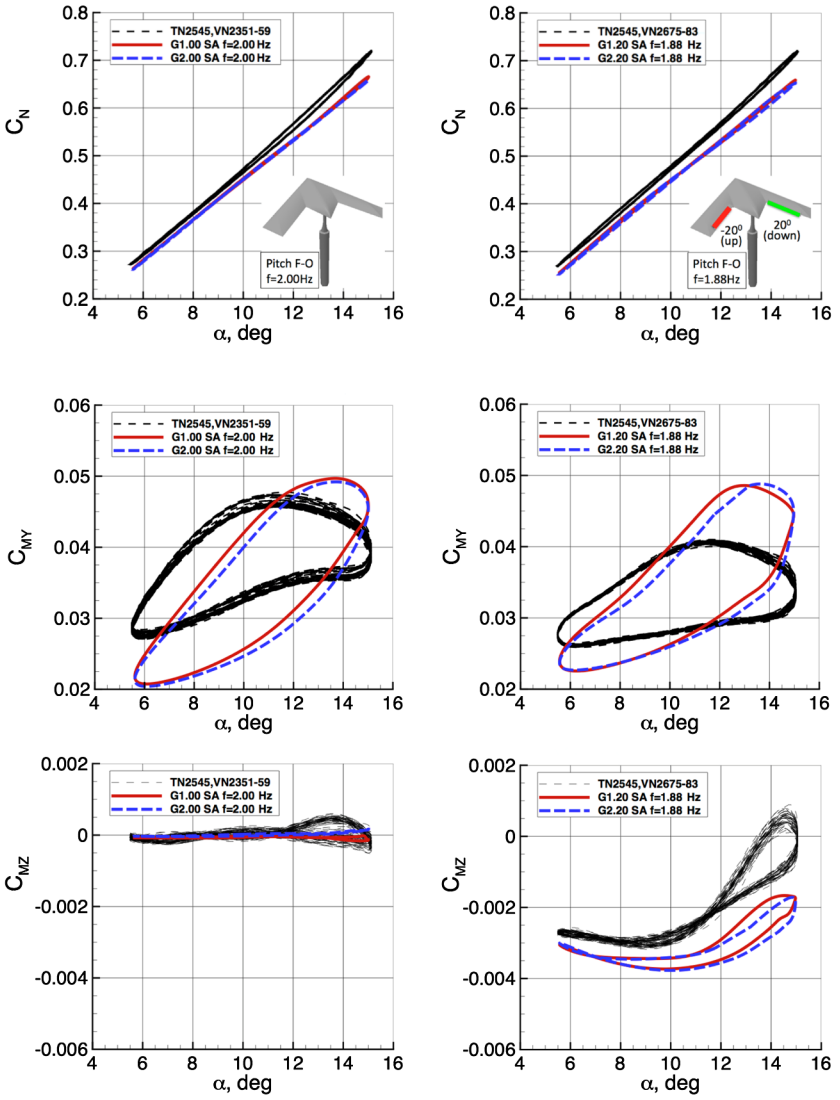

Fig. 51 Effect of grid density under high-frequency pitch oscillation ($k_P = 0.12$), $\Theta_0 = 10.3$ deg, and $\Delta\Theta = \pm 4.7$ deg. CS0 (left) and CS20 (right). $M_\infty = 0.14$, $Re_{\text{cref}} = 1.5$ million. NASA USM3D/SA, grids 1 and 2.

Table 8 ΔC_{MY} and ΔC_{MZ} coefficients for DLR-F19 undergoing pitch oscillation at $\Theta_0 = 10.3$ deg

		CS0			CS20		
			USM3D/SA			USM3D/SA	
k_P	ΔC_M	TN2545 [21]	G1.00	G2.00	TN2545 [20]	G1.20	G2.20
0.06	ΔC_{MY}	−0.007	−0.0097	−0.0092	−0.0062	−0.0073	−0.0065
	ΔC_{MZ}	0.000	0.0000	0.0000	0.0002	−0.0004	−0.0004
0.12	ΔC_{MY}	−0.013	−0.0169	−0.0160	−0.012	−0.0143	−0.0123
	ΔC_{MZ}	0.000	0.0000	0.0000	0.0002	−0.0003	−0.0004

Table 9 Common dynamic test cases for YAW F-O. SACCON DLR-F19. $\Phi_0 = 0$ deg, $\Psi_0 = 0$ deg

DLR TN2545 [21]	LOB/LIB, deg	ROB/RIB, deg	Θ_0, deg	$\Delta\Psi$, deg	f, Hz	$k_Y\ 2\pi f \cdot b_{\text{ref}}/U_\infty$	M_∞	Re_{cref}, million
2270-78	— —	— —	10.1	5	1	0.10	0.146	1.57
2279-87	— —	— —	10.1	5	2	0.19	0.146	1.57
2162-70	−20/ − 20	+20/ + 20	10.1	5	0.94	0.10	0.138	1.49
2171-79	−20/ − 20	+20/ + 20	10.1	5	1.88	0.19	0.138	1.49

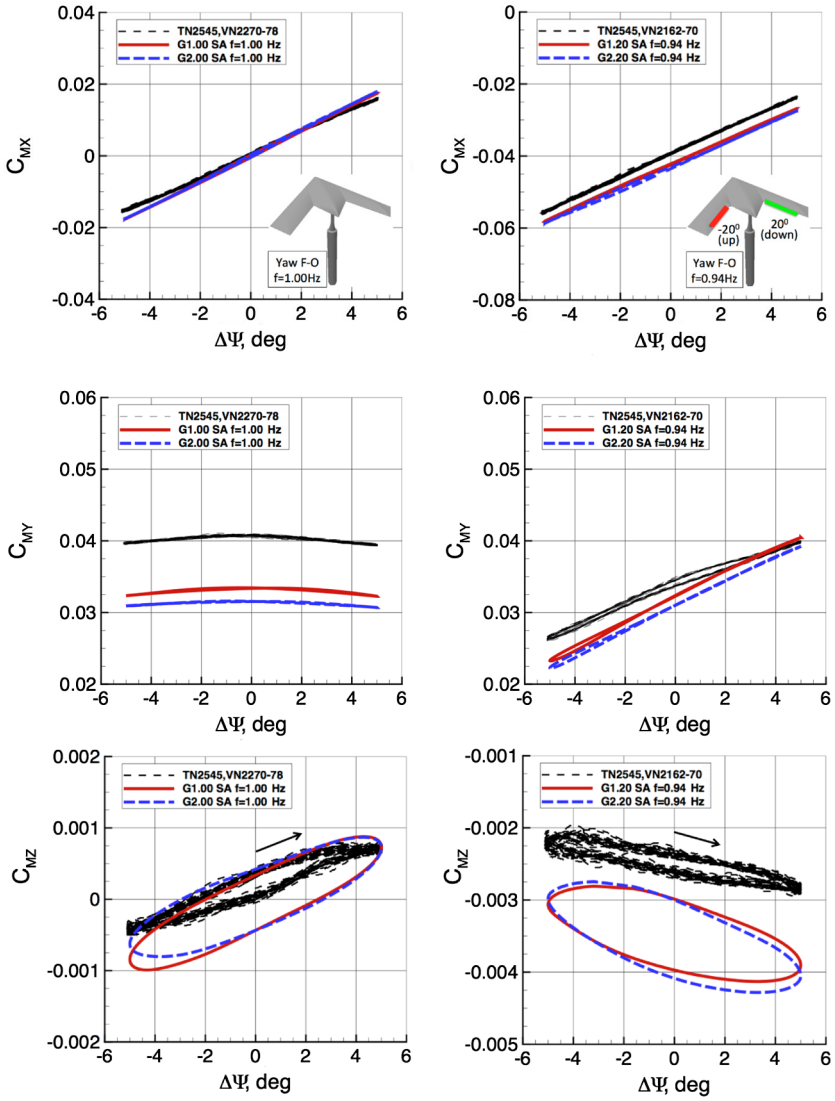

Fig. 52 Effect of grid density under low-frequency yaw oscillation ($k_Y = 0.10$), $\Theta_0 = 10.1$ deg, and $\Delta\Psi = \pm 5.0$ deg. CS0 (left) and CS20 (right). $M_\infty = 0.14$, $Re_{\text{cref}} = 1.5$ million. NASA USM3D/SA, grids 1 and 2.

stationary post support sting and the oscillating SACCON configuration. For current computational results, the SACCON was supported by the 15 deg cranked yaw-link sting, and pitch oscillations were imposed as a solid-body rotation of the entire grid, which contained no relative motions between the sting and the wing.

The pitch oscillation correlations are shown for low frequency ($k_P = 0.06$) in Fig. 50 and high frequency ($k_P = 0.12$) in Fig. 51. These figures portray the effect of grid density G1 and G2 using the USM3D/SA model on the aerodynamic response to the motion, which manifests as hysteresis loops for C_N, C_{MY}, and C_{MZ} that oscillate in pitch in the counterclockwise direction at 5.6 deg $\leq \alpha \leq$ 15 deg. The effect of the grid density is noticeable but not large. The choice of turbulence model has a much greater impact, as demonstrated by Frink et al. [17]. For computing dynamic stability derivatives, the shape of the hysteresis curves is the indicator of dynamic stability characteristics. In particular, the width of the hysteresis loop $\Delta C_M = (C_{M+} - C_{M-})$ at $\alpha_0 = 10.3$ deg is proportional to the dynamic damping coefficient [18]. Here, C_{M+} is the moment coefficient across α_0 with increasing angle, and C_{M-} is the moment coefficient across α_0 with decreasing angle. (The vertical offsets observed between the experiment and CFD are related to the static offset that often occurs from turbulence model or grid effects; these have no bearing on the dynamic stability derivative.) For this case, the ΔC_{MY} or ΔC_{MZ} at $\alpha_0 = \Theta_0 =$ 10.3 deg are presented in Table 8. Because of the counterclockwise direction of pitch and yaw hysteresis, the increments in moments are negative, which indicate damping. In general, the pitch damping from CFD tends to be slightly higher than the experiment but is still reasonably close. The yaw damping due to pitch oscillation is essentially negligible.

2. *Forced Oscillation in Yaw (NASA USM3D)*

The AVT-201 common test cases for forced oscillation in yaw are listed in Table 9. Two reduced frequencies for yaw oscillation ($k_Y = 0.10$ and 0.19) are assessed for $\Delta\Psi = \pm 5$ deg sinusoidal oscillations at a pitch angle of $\Theta_0 = 10.1$ deg, with and without control surface deflections. The run numbers from the corresponding correlation DLR's wind-tunnel [21] dataset are listed in the first column. The Mach and Reynolds numbers are adjusted in the computations to correspond to their respective test conditions. The appropriate grids were selected from the results of the static study.

Low- and high-frequency oscillations of $\Delta\Psi = \pm 5$ deg about initial angles of $\Theta_0 = 10.1$ deg and $\Psi_0 = 0$ deg are investigated for $k_Y = 2\pi f \cdot b_{\text{ref}}/V_\infty$ of 0.10 and 0.19. These reduced frequencies correspond, respectively, to 1.00 and 2.00 Hz for CS0, and 0.94 and

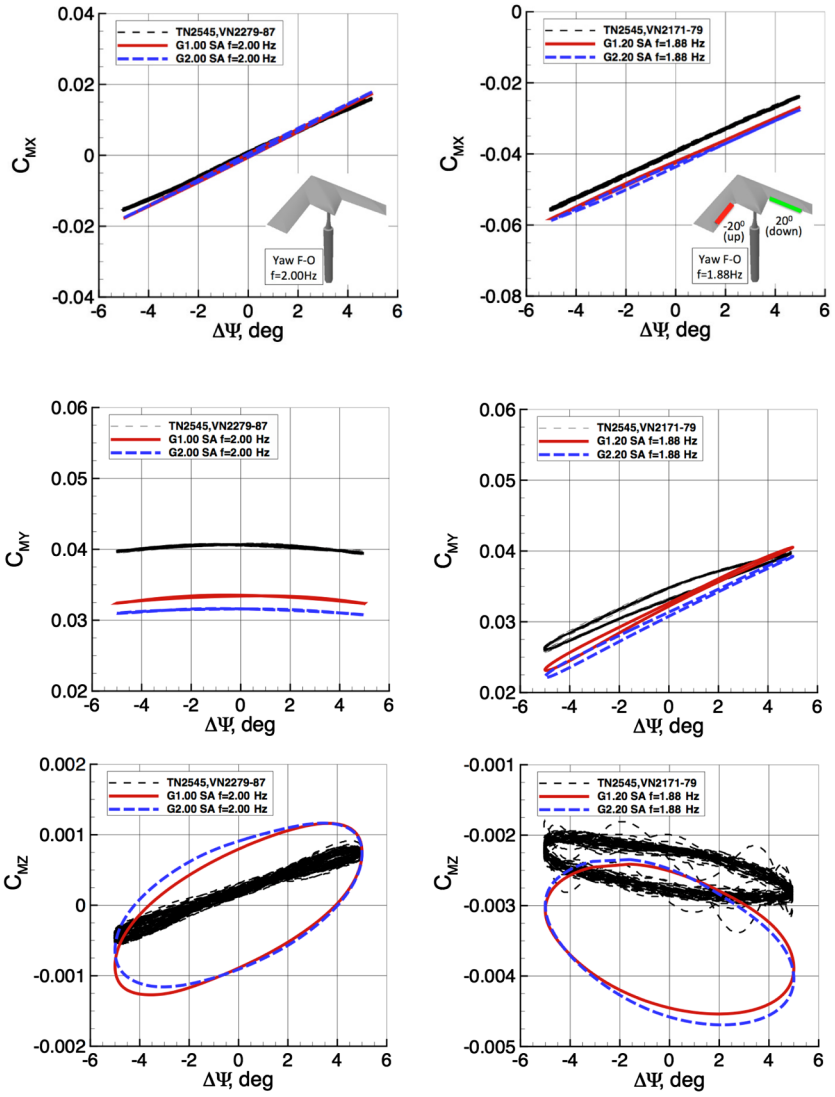

Fig. 53 Effect of grid density under high-frequency yaw oscillation ($k_Y = 0.19$), $\Theta_0 = 10.1$ deg, and $\Delta\Psi = \pm 5.0$ deg. CS0 (left) and CS20 (right). $M_\infty = 0.14$, $Re_{\text{cref}} = 1.5$ million. NASA USM3D/SA, grids 1 and 2.

1.88 Hz for CS20 cases. The SACCON configuration was supported by the 15 deg cranked yaw-link sting for both the wind-tunnel [21] and CFD models, with no relative motion between the sting and the wing during yaw oscillations.

The yaw oscillation correlations are shown for the low frequency ($k_Y = 0.10$) in Fig. 52 and the high frequency ($k_Y = 0.19$) in Fig. 53. These figures portray the effect of grid density G1 and G2 using the USM3D/SA model on the aerodynamic response to the motion, which manifests as hysteresis loops for C_{MX}, C_{MY}, and C_{MZ} that oscillate in the clockwise direction within -5 deg $\le \Psi \le +5$ deg. As with the pitch oscillation, the effect of grid density for yaw forced-oscillation sinusoidal motion (referred to as F-O) is observed to be nominal.

The width of the hysteresis loops ΔC_{MX} and ΔC_{MZ}, where $\Delta C_M = (C_{M+} - C_{M-})$ at $\Psi_0 = 0$, are collected in Table 10. Here, C_{M+} the respective yawing moment coefficient as the aircraft yaws nose right across $\Psi = 0$. Similarly C_{M-} is the yawing moment coefficient as the aircraft yaws nose left across $\Psi = 0$. The levels of ΔC_{MX} and ΔC_{MZ} are very small due to the absence of any vertical surfaces. Although very small, the ΔC_{MX} does change sign from negative to positive between CS0 and CS20, indicating a tendency to lose roll damping. In general, the positive increments correspond to

Table 10 ΔC_{MX} and ΔC_{MZ} coefficients for DLR-F19 undergoing yaw oscillation at $\Theta_0 = 10.1$ deg

		CS0			CS20		
			USM3D/SA			USM3D/SA	
k_Y	ΔC_M	TN2545 [21]	G1.00	G2.00	TN2545 [20]	G1.20	G2.20
0.10	ΔC_{MX}	0.000	−0.0007	−0.0007	0.000	0.0003	0.0005
	ΔC_{MZ}	0.0003	0.0008	0.0009	0.0003	0.0010	0.0011
0.19	ΔC_{MX}	0.000	−0.0010	−0.0010	0.000	0.0004	0.0008
	ΔC_{MZ}	0.000	0.0017	0.0018	0.0007	0.0019	0.0021

Table 11 Dynamic test cases for roll F-O: SACCON DLR-F17, $\Phi_0 = 0$ deg, $\Psi_0 = 0$ deg

NASA T134 [12]	Θ_0, deg	$\Delta\Phi$, deg	f, Hz	$k_R\ 2\pi f \cdot b_{\text{ref}}/U_\infty$
17	10, 20	5	0.24	0.063
18	10, 20	5	0.36	0.095
19	10, 20	5	0.44	0.116
20	10, 20	5	0.55	0.145
22	10, 20	5	0.66	0.174
25	10, 20	5	0.86	0.227
12	10, 20	5	1.00	0.264

clockwise oscillation loops that represent propelling, and negative increments correspond to counterclockwise loops that indicate damping. In general, the ΔC_M from CFD is approaching three times larger than in the experiment for the yaw F-O. Although no specific reason has been discerned, this comparison is between two small numbers. Hence, in the absence of any vertical control surfaces and the small projected area of wing thickness, these increments are highly sensitivity to the smallest perturbations. In contrast, the previous pitch and subsequent roll F-O results experience a strong forcing function from the interactions of larger aerodynamic surface projections with motion.

3. *Forced Oscillation in Roll (NASA USM3D)*

The roll oscillation cases for the AVT-161 DLR-F17 configuration are listed in Table 11. These consist of prescribing sinusoidal roll oscillations of $\Delta\Phi = \pm 5$ deg at seven frequencies for $\Theta_0 = 10$ and 20 deg. The corresponding run numbers from the NASA dataset are listed in the first column. The NASA wind-tunnel data Mach and Reynolds numbers are $M_\infty = 0.053$ and $Re_{\text{cref}} = 0.375$ million.

Solutions were computed for seven frequencies of roll oscillation between $\Delta\Phi = \pm 5$ deg at angles of attack of $\alpha_0 = 10$ and 20 deg. The reduced frequencies $k_R = 2\pi f \cdot b_{\text{ref}}/V_\infty$ ranged between 0.063 and 0.264 ($f = 0.24$ to 1.00 Hz). For the sake of brevity, only two of these cases are presented in Figs. 54 and 55 to document the roll F-O hysteresis behavior and degree of correlation with the experiment in a manner consistent with previous pitch and yaw results. In the work of Murphy et al. [51], these solutions have been used to explore the creation of reduced-order models from CFD data using system identification techniques.

The plots of C_{MX}, C_{MZ}, and C_Y vs $\Delta\Phi$ presented in Figs. 54 and 55 correspond to $k_R = 0.145$ and 0.264 ($f = 0.55$ and 1.00 Hz), respectively. The left column portrays the $\alpha_0 = 10$ deg results, and the right column portrays the $\alpha_0 = 20$ deg results. For each frequency, dynamic damping is evidenced in the roll and yaw from the counterclockwise oscillation loops and propelling (nondamping) for the side force as evidenced by clockwise loops. It should be mentioned that some vertical offsets present in the experimental data

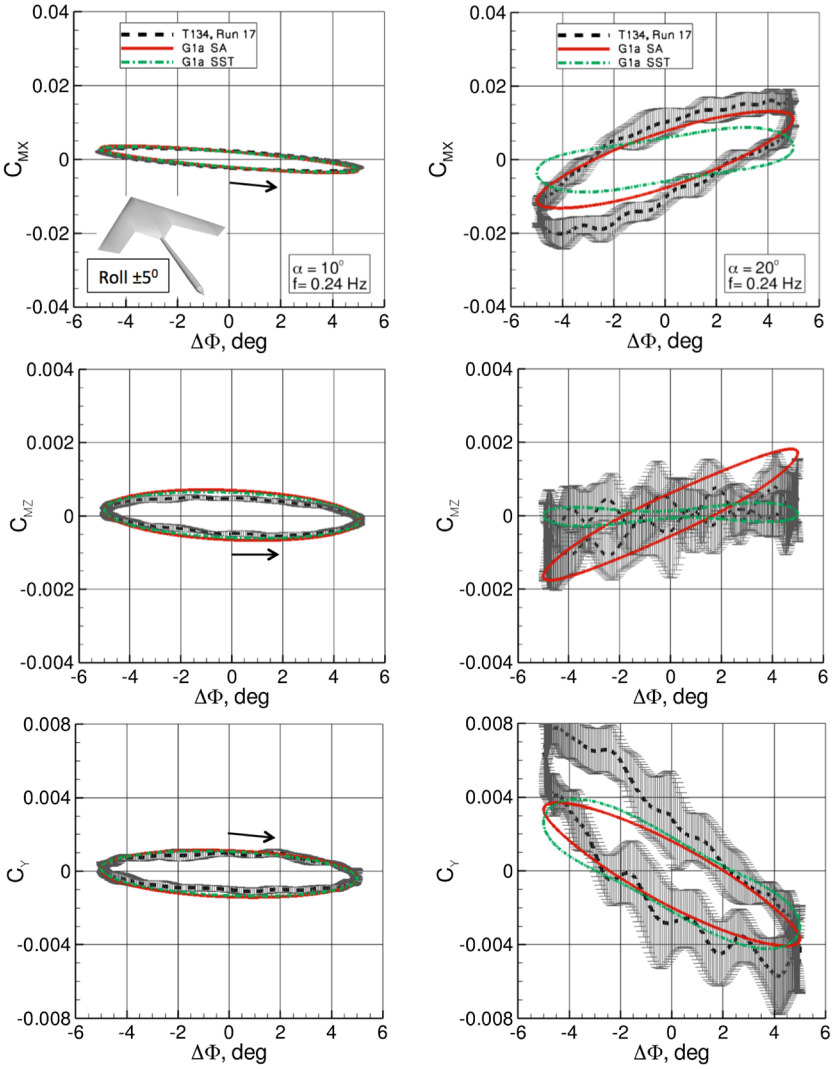

Fig. 54 Effect of turbulence model under roll oscillation, $f = 0.24$ Hz, $k_R = 0.063$, and $\Delta\Phi = \pm 5$ deg: $\alpha = 10$ deg (left), and $\alpha = 20$ deg (right). $M_\infty = 0.14$, $Re_{\text{cref}} = 1.40$ million. NASA USM3D/SA/SST, grid 1a.

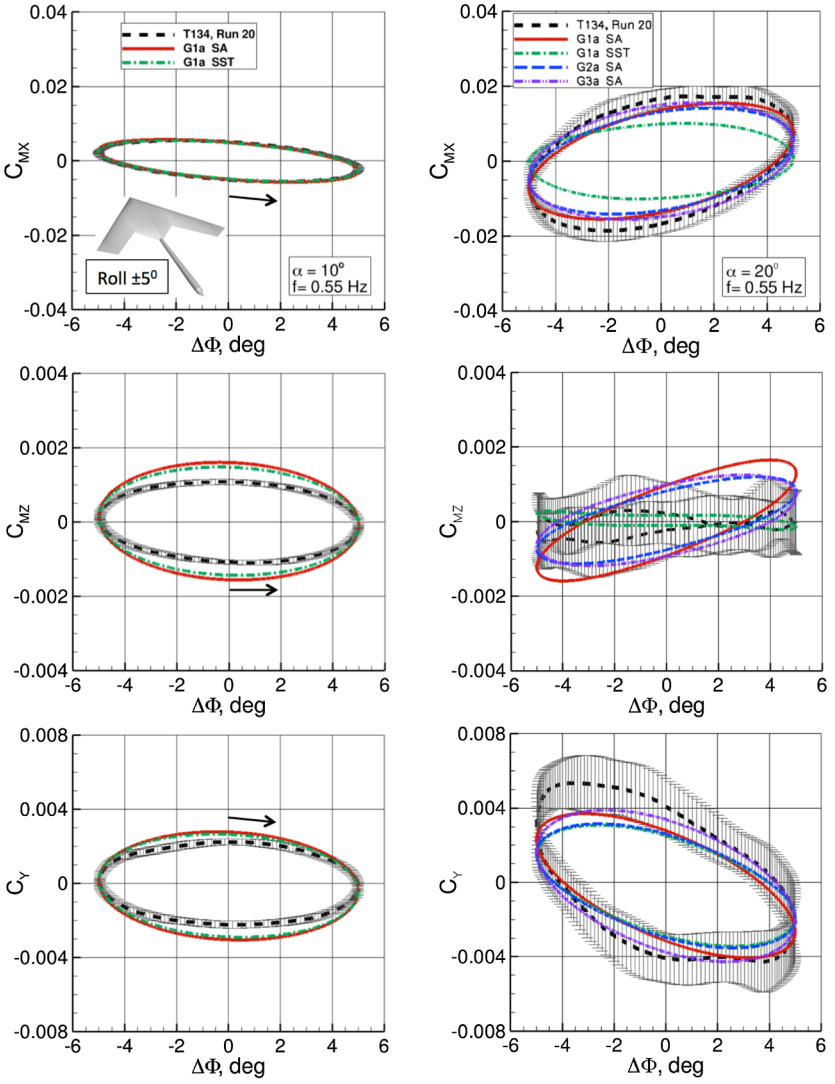

Fig. 55 Effect of grid and turbulence model on DLR-F17 lateral/directional coefficients under forced roll oscillation, $f = 0.55$ Hz, $k_R = 0.145$, and $\Delta\Phi = \pm 5$ deg: $\alpha = 10$ deg (left), and $\alpha = 20$ deg (right). $M_\infty = 0.14$, $Re_{cref} = 1.40$ million. NASA USM3D/SA/SST, grids 1a and 2a.

at a zero roll angle, typically caused by small asymmetries in the model geometry and possible flow angularity, have been subtracted out to facilitate more consistent comparisons of shape with the CFD predictions; see, as well, work by Vicroy et al. [12] The vertical offset is computed as the average of the two zero-axis crossing values. The NASA wind-tunnel data in the figures also include variation bars denoting the standard deviation of flow unsteadiness.

The effect of the SA/SST turbulence models on the coarsest grid G1a from Table 2 is shown in Figs. 54–56. In general, for $\alpha_0 = 10$ deg, the CFD oscillation loops are in close agreement with the relatively steady experimental data and the effect of turbulence model is small, but less so at $\alpha_0 = 20$ deg. Referring back to the static data in Fig. 42, $\alpha = 10$ deg corresponds to a more well-behaved prestall condition, whereas $\alpha = 20$ deg falls within a very unsteady poststall flow condition. Excellent correlations are exhibited in Fig. 54 at $\alpha = 10$ deg for C_{MX} across the frequency range, correctly predicting the increase in roll damping with increasing roll frequency. Although the trends with increasing frequency are reflected correctly for C_{MZ}, as well as C_Y at $\alpha_0 = 10$ deg, there is a slight overprediction of the dynamic effect. At $\alpha_0 = 20$ deg, the experimental data display significantly more unsteadiness. As might be expected, the CFD solutions produce a more varied correlation with the data. An impact of the turbulence model can also be observed at $\alpha_0 = 20$ deg, with the SA model being in closer agreement with the mean value of the experimental data than the SST model.

The effects of grids G1a/G2a/G3a from Table 4 using the SA turbulence model at $\alpha_0 = 20$ deg are investigated in Fig. 54 (right) for the midfrequency case $f = 0.55$ Hz. Although grid refinement does produce better correlations with the experimental data, the dominant effect comes from the SST turbulence model. An investigation of the impact of these CFD solution uncertainties on the creation of reduced-order models constructed by system identification techniques was reported by Murphy et al. [51]. There, two methods were presented (harmonic analysis and a two-step linear regression) for estimating mathematical models useful for stability and control analysis that can be applied to both CFD simulations and wind-tunnel measurements. This approach offers a model structure that can accommodate unsteady aerodynamic behavior of the DLR-F17 and characterize model parameter uncertainty. A regression analysis of the CFD/SST simulated data resulted in a steady-flow damping parameter in statistical agreement with the wind tunnel and CFD/SA cases, but not for the unsteady term. For the CFD/SST case, the unsteady term was statistically different and with a much larger uncertainty bound than either the wind-tunnel or CFD/SA cases. Time history comparisons in the work by Murphy et al. [51] confirmed the reduced-order model agreement between the wind-tunnel and CFD/SA models, but the CFD/SST case showed the added uncertainty due to turbulence model selection.

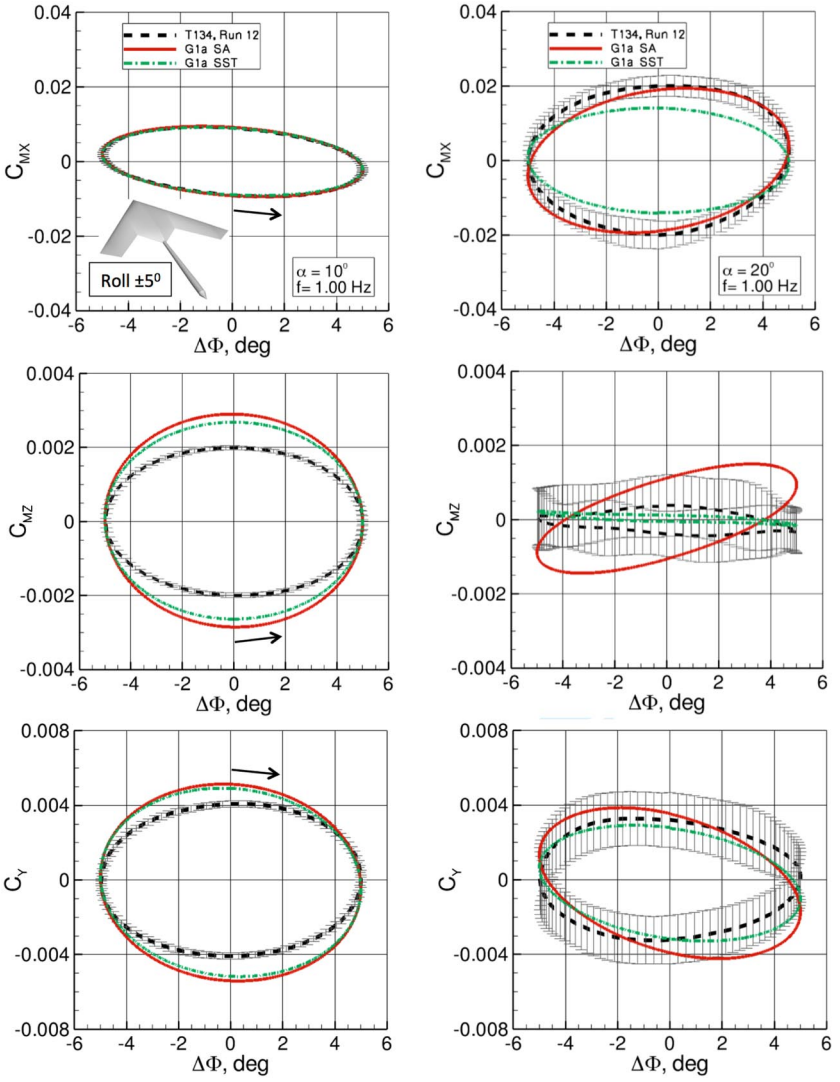

Fig. 56 Effect of turbulence model on DLR-F17 lateral/directional coefficients under forced roll oscillation, $f = 1.00$ Hz, $k_R = 0.264$, and $\Delta\Phi = \pm 5$ deg: $\alpha = 10$ deg (left), and $\alpha = 20$ deg (right). $M_\infty = 0.14$, $Re_{\text{cref}} = 1.40$ million. NASA USM3D/SA/SST, grid 1a.

V. Conclusions

The state of aerodynamic stability and control predictive capability of a time-accurate RANS methodology was investigated for a 53 deg swept UCAV configuration with control surface deflections. The vehicle aerodynamics was dominated by the complex nonlinear physics of round leading-edge vortex flow separation. Correlations with wind-tunnel data were made for static longitudinal/lateral sweeps and at varying frequencies of prescribed roll/pitch/yaw sinusoidal motion for the vehicle operating with and without control surfaces. The ultimate purpose for these investigations was to provide data and insight to researchers who were developing techniques for augmenting flight simulation models from low-speed CFD predictions of aircraft traversing nonlinear regions of a flight envelope

To this end, simulations have been done using the unstructured/hybrid grid-based DLR TAU code, the structured (multiblock) grid-based NLR solver ENSOLV, and the unstructured grid-based NASA USM3D Code. The simulation results have been compared among each other, as well as to the available experimental data.

These comparisons led to the following conclusions:

1) All three state-of-the-art CFD methods were well capable of predicting the dominant flow features on the DLR-F19 configuration. The investigations included assessments of grid and turbulence model sensitivities with control surfaces deflected asymmetrically and undeflected. The effect of control surface deflection on the three-axis moment coefficients was modeled with comparable accuracy to that with undeflected surfaces for angle of attack and sideslip sweeps. The agreement between all methods was good. The SA turbulence model was selected as the most consistent approach for the full range of the test matrix

2) However, to simulate the flow features at higher angles of attack realistically (i.e., α greater than 15 deg), more advanced turbulence models, such as the RSM, were required. For angles of attack at α smaller than 15 deg, more conventional turbulence models were sufficient, especially when these simulations were used for stability and control database generation.

3) For symmetric onflow conditions (AOS equals 0 deg) and low AOAs, the stability and control database for the full-span configuration may well have been reconstructed from the half-span integral data. This was applicable for the BL as well as for configuration with control surface deflections. This would reduce the computing time and costs by a factor of two.

4) For an accurate comparison with wind-tunnel data, the modeling of the belly sting support was essential, since it was found that the sting support not only gave rise to an unsteady wake on the lower side of the configuration but also had an effect on the flow on the upper side of the configuration.

5) The roll/pitch/yaw forced oscillation computations produced dynamic stability characteristics consistent with that from the experimental data. Future research will, in addition to better understanding and modeling of the flow physics, focus more on such simulations and how they can efficiently be used to generate a stability and control database.

Acknowledgments

The authors from the DLR would like to thank the German Ministry of Defence (MoD) and the Federal Office of Bundeswehr Equipment, Information Technology, and In-Service Support (BAAINBw) for their support for the military research at the DLR and the support to attend the NATO STO/AVT Task Group meetings. The author from NASA would like to express his appreciation to the Vehicle Systems Safety Technologies project under the NASA Aviation Safety Program for providing the funding for this effort. Part of this work has been conducted under the programmatic research funding "Kennis voor Beleid en Toepassing" of the National Aerospace Laboratory/NLR. The author from NASA would also like to thank Ed Parlette of ViGYAN, Inc., for generating the computational grids. Also, thanks are offered to Greg Power and Chris Robinson at Arnold Engineering and Development Center, as well as Mohagna Pandya of NASA Langley Research Center, for invaluable help with application of the fluid dynamics/computational analysis of dynamically responsive environments framework. All authors would like to thank the whole team from DLR, German Aerospace Center (DLR) and German–Dutch Wind Tunnels in Brunswick, Germany, for gathering the data with the DLR-F19 model configuration. Furthermore, we would like to thank all the members of NATO STO AVT-201 Task Group on "Extended Assessment of Stability and Control Prediction Methods for NATO Air Vehicles" for their support and collaborative work within the North Atlantic Treaty Organization (NATO) Science and Technology Organization (STO)/Applied Vehicle Technology (AVT) research community.

References

[1] Hummel, D., and Redeker, G., "A New Vortex Flow Experiment For Computer Code Validation," *RTO AVT Meeting Proceedings*, RTO-MP-069-1, 2003, pp. 8-1–8-31.

[2] Hummel, D., "The Second International Vortex Flow Experiment (VFE-2): Objectives and First Results," *Journal of Aerospace Engineering*, Vol. 220, No. 6, 2006, pp. 559–568.

[3] Hummel, D., "Review of the Second International Vortex Flow Experiment (VFE-2)," *46th AIAA Aerospace Sciences Meeting and Exhibit*, AIAA Paper 2008-0377, Jan. 2008.

[4] Schütte, A., and Lüdeke, H., "Numerical Investigations on the VFE-2 65-Degree Rounded Leading Edge Delta Wing Using the Unstructured DLR-TAU-Code," *Aerospace Science and Technology*, Vol. 24, No. 1, Jan.–Feb. 2013, pp. 56–65. doi:10.1016/j.ast.2012.03.002

[5] Fritz, W., and Cummings, R. M., "What was Learned from the Numerical Simulations for the VFE-2," *46th AIAA Aerospace Sciences Meeting and Exhibit*, AIAA Paper 2008-0399, 2008. doi:10.2514/6.2008-399

[6] Luckring, J. M., and Hummel, D., "What was Learned from the New VFE-2 Experiments?" *46th AIAA Aerospace Sciences Meeting and Exhibit*, AIAA Paper 2008-0383, 2008. doi:10.2514/6.2008-383

[7] Hummel, D., and Lamar, J. (eds.), "Understanding and Modeling Vortical Flows to Improve the Technology Readiness Level for Military Aircraft," NATO Research and Technology Organization/Applied Vehicle Technology, AVT-113 Task Group Final Rept. RTO-TR-AVT-113 AC/323(AVT-113)TP/246, Oct. 2009.

[8] Boelens, O. J., Babcock, K. J., Elmilgui, A., Abdol-Hamid, K. S., and Massey, S. J., "Comparison of Measured and Block Structured Simulation Results for the F-16XL Aircraft," *Journal of Aircraft*, Vol. 46, No. 2, 2009, pp. 377–384. doi:10.2514/1.35064

[9] Görtz, S., Jirásek, A., Morton, S. A., McDaniel, D. R., Cummings, R. M., Lamar, J. E., and Abdol-Hamid, K. S., "Standard Unstructured Grid Solutions for Cranked Arrow Wing Aerodynamics Project International F-16XL," *Journal of Aircraft*, Vol. 46, No. 2, 2009, pp. 385–408. doi:10.2514/1.35163

[10] Fritz, W., Davis, M. B., Karman, S. L., and Michal, T., "Reynolds-Averaged Navier–Stokes Solutions for the CAWAPI F-16XL Using Different Hybrid Grids," *Journal of Aircraft*, Vol. 46, No. 2, 2009, pp. 409–422. doi:10.2514/1.35106

[11] Schütte, A., Boelens, O. J., Oehlke, M., Jirásek, A., and Loeser, T., "Prediction of the Flow Around the X-31 Aircraft Using Three Different CFD Methods," *Journal of Aerospace Science and Technology*, Vol. 20, No. 1, July–Aug. 2012, pp. 21–37. doi:10.1016/j.ast.2011.07.014

[12] Vicroy, D. D., Loeser, T. D., and Schütte, A., "Static and Forced-Oscillation Tests of a Generic Unmanned Combat Air Vehicle," *Journal of Aircraft*, Vol. 49, No. 6, 2012, pp. 1558–1583. doi:10.2514/1.C031501

[13] Roosenboom, E. W. M., Konrath, R., Schröder, A., Pallek, D., Otter, D., Morgand, S., Gilliot, A., Monnier, J. C., Le Roy, J. F., Geiler, C., and Pruvost, J., "Stereoscopic Particle Image Velocimetry Flowfield Investigation of an Unmanned Combat Air Vehicle," *Journal of Aircraft*, Vol. 49, No. 6, 2012, pp. 1584–1596. doi:10.2514/1.C031587

[14] Cummings, R. M., and Schuette, A., "Integrated Computational/Experimental Approach to Unmanned Combat Air Vehicle Stability and Control Estimation," *Journal of Aircraft*, Vol. 49, No. 6, 2012, pp. 1542–1557. doi:10.2514/1.C031430

[15] Cummings, R. M., and Schuette, A. (eds.), "Assessment of Stability and Control Prediction Methods for NATO Air and Sea Vehicles," NATO Research and Technology Organization/Applied Vehicle Technology, AVT-161 Task Group Final Rept. RTO-TR-AVT-161 AC/323(AVT-161)TP/440, Sept. 2012.

[16] Schütte, A., Hummel, D., and Hitzel, S. M., "Flow Physics Analyses of a Generic Unmanned Combat Aerial Vehicle Configuration," *Journal of Aircraft*, Vol. 49, No. 6, 2012, pp. 1638–1651. doi:10.2514/1.C031386

[17] Frink, N. T., Tormalm, M., and Schmidt, S., "Three Unstructured Computational Fluid Dynamics Studies on Generic Unmanned Combat Aerial Vehicle," *Journal of Aircraft*, Vol. 49, No. 6, 2012, pp. 1619–1637. doi:10.2514/1.C031383

[18] Cummings, R. M., Schuette, A., and Huebner, A.-R., "Overview of Stability and Control Estimation Methods from NATO STO Task Group AVT-201," *51st AIAA Aerospace Sciences Meeting including the New Horizons Forum and Aerospace Exposition*, AIAA Paper 2013-0968, 2013.

[19] Cummings, R. M., and Schuette, A., "The NATO STO AVT-201 Task Group on Extended Assessment of Stability an Control Prediction Methods for NATO Air Vehicles," *32nd AIAA Applied Aerodynamics Conference*, AIAA Paper 2014-2000, June 2014.

[20] Huber, K., Vicroy, D. D., Schütte, A., and Hübner, A.-R., "UCAV Model Design Investigations and Static Low Speed Wind Tunnel Experiments to Estimate Control Device Effectiveness and S&C Capabilities," *32nd AIAA Applied Aerodynamics Conference*, AIAA Paper 2014-2002, June 2014.

[21] Vicroy, D. D., Huber, K., Loeser, T., and Rohlf, D., "Dynamic Low Speed Wind Tunnel Experiments and S&C Analyses of a Generic High Swept UCAV Configurations," *32nd AIAA Applied Aerodynamics Conference*, AIAA Paper 2014-2003, June 2014.

[22] Rein, M., Irving, J., Rigby, G., and Birch, T., "High Speed Static Experimental Investigations on a Generic UCAV to Estimate Control Device Effectiveness and S&C Capabilities," *32nd AIAA Applied Aerodynamics Conference*, AIAA Paper 2014-2004, June 2014.

[23] Liersch, C., and Huber, K., "Conceptual Design and Aerodynamic Analyses of a Generic UCAV Configuration," *32nd AIAA Applied Aerodynamics Conference*, AIAA Paper 2014-2001, June 2014.

[24] Bergmann, A., Huebner, A.-R., and Loeser, T., "Experimental and Numerical Research on the Aerodynamics of Unsteady Moving Aircraft," *Progress in Aerospace Sciences*, Vol. 44, No. 2, Feb. 2008, pp. 121–137. doi:10.1016/j.paerosci.2007.10.006

[25] Galle, M., Gerhold, T., and Evans, J., "Technical Documentation of the DLR TAU-Code," DLR Internal Rept. DLR-IB 233-97/A43, 1997.

[26] Gerhold, T., Galle, M., Friedrich, O., and Evans, J., "Calculation of Complex Three-Dimensional Configurations Employing the DLR TAU-Code," AIAA Paper 1997-0167, Jan. 1997.

[27] Gerhold, T, "Overview of the Hybrid RANS Code TAU," *MEGA-FLOW — Numerical Flow Simulations for Aircraft*, Vol. 89, edited by Kroll, N., and Fassbender, J., Notes on Numerical Fluid Mechanics Series, Springer, Berlin, 2005, pp. 81–92.

[28] Schwamborn, D., Gerhold, T., and Heinrich, R., "The DLR TAU-Code: Recent Applications in Research and Industry," *Invited Lecture in Proceedings on CD of the European Conference on Computational Fluid Dynamics ECCOMAS CDF 2006*, edited by Wesseling, P., Oñate, J. P., and Périaux, J., The Netherlands, 2006.

[29] Spalart, P. R., and Allmaras, S. R., "A One-Equation Turbulence Model for Aerodynamic Flows," *Recherche Aerospatiale*, No. 1, 1994, pp. 5–21.

[30] Allmaras, S. R., Johnson, F. T., and Spalart, P. R., "Modifications and Clarifications for the Implementation of the Spalart–Allmaras

Turbulence Model," *Seventh International Conference on Computational Fluid Dynamics (ICCFD7)*, Paper. ICCFD7-1902, Big Island, HI, July 2012.

[31] Eisfeld, B., and Brodersen, O., "Advanced Turbulence Modelling and Stress Analysis for the DLR-F6 Configuration," *23rd AIAA Applied Aerodynamics Conference*, AIAA Paper 2005-4727, June 2005.

[32] Cecora, R.-D., Eisfeld, B., Probst, A., Crippa, S., and Radespiel, R., "Differential Reynolds Stress Modeling for Aeronautics," *50th AIAA Aerospace Sciences Meeting including the New Horizons Forum and Aerospace Exposition*, AIAA Paper 2012-0465, Jan. 2012.

[33] Kalitzin, G., "Validation, and Development of Two-Equation Turbulence Models," *Validation of CFD Codes, and Assessment of Turbulence Models*, Vol. 58, edited by Haase, W., Chaput, E., Elsholz, E., Leschziner, M. A., and Müller, U. R., Notes on Numerical Fluid Mechanics Series, Vieweg, Brunswick, Germany, 1997, pp. 319–326.

[34] Kalitzin, G., and Iaccarino, G., "Turbulence Modeling in an Immersed-Boundary RANS Method," *Annual Research Briefs*, Stanford Univ., Center for Turbulence Research, Stanford, CA, 2002, pp. 415–426.

[35] Boerstoel, J. W., Kassies, A., Kok, J. C., and Spekreijse, S. P., "ENFLOW, a Full-Functionality System of CFD Codes for Industrial Euler/Navier–Stokes Flow Computations," National Aerospace Laboratory/NLR Rept. TP-96286U, Amsterdam, 1996.

[36] Kok, J. C., "Resolving the Dependence on Free-Stream Values for the k-ω Turbulence Model," National Aerospace Laboratory/NLR Rept. NLR-TP-99295, Amsterdam, 1999.

[37] Brandsma, F. J., Kok, J. C., Dol, H. S., and Elsenaar, A., "Leading Edge Vortex Flow Computations and Comparison with DNW-HST Wind Tunnel Data," National Aerospace Laboratory/NLR Rept. NLR-TP-2001-238, Amsterdam, 2001.

[38] Dol, H. S., Kok, J. C., and Oskam, B., "Turbulence Modeling for Leading-Edge Vortex Flows," AIAA Paper 2002-0843, 2002.

[39] Kok, J. C., Dol, H. S., Oskam, B., and van der Ven, H., "Extra-Large Eddy Simulation of Massively Separated Flows," National Aerospace Laboratory/NLR Rept. NLR-TP-2003-200, Amsterdam, 2003.

[40] Kok, J. C., Soemarwoto, B. I., and van der Ven, H., "X-LES Simulations Using a High-Order Finite-Volume Scheme," *Advances in Hybrid RANS–LES Modelling*, Vol. 97, edited by Peng, S. H. , and Haase, W. , Notes on Numerical Fluid Mechanics, and Multidisciplinary Design, Springer, New York, 2008, pp. 87–96.

[41] Frink, N. T., "Tetrahedral Unstructured Navier–Stokes Method for Turbulent Flows," *AIAA Journal*, Vol. 36, No. 11, 1998, pp. 1975–1982. doi:10.2514/2.324

[42] Girimaji, S. S., "Fully Explicit and Self-Consistent Algebraic Reynolds Stress Model," *Theoretical and Computational Fluid Dynamics*, Vol. 8, No. 6, Nov. 1996, pp. 387–402. doi:10.1007/BF00455991

[43] Shih, T.-H., Zhu, J., and Lumley, J. L., "A New Reynolds Stress Algebraic Equation Model," *Computer Methods in Applied Mechanics and Engineering*, Vol. 125, Nos. 1–4, Sept. 1995, pp. 287–302. doi:10.1016/0045-7825(95)00796-4

[44] Power, G. D., and Calahan, J. A., "A Flexible System for Analysis of Bodies in Relative Motion," AIAA Paper 2005-5120, June 2005.

[45] Pandya, M. J., Frink, N. T., Abdol-Hamid, K. S., Samareh, J. A., Parlette, E. B., and Taft, J. R., "Enhancements to TetrUSS for NASA Constellation Program," *Journal of Spacecraft and Rockets*, Vol. 49, No. 4, 2012, pp. 617–631. doi:10.2514/1.A32089

[46] Centaur Software, Software Package, Ver. centaur10.0, CentaurSoft, Austin, TX, Jan. 2013, http://www.Centaursoft.com [retrieved 2016].

[47] Boelens, O. J., "CFD Analysis of the Flow Around the X-31 Aircraft at High Angle of Attack," AIAA-Paper 2009-3628, 2009.

[48] Boelens, O. J., Badcock, K. J., Görtz, S., Morton, S., Fritz, W., Karman, S. L., Jr., Michal, T., and Lamar, J. E., "Description of the F-16XL Geometry and Computational Grids used in CAWAPI," *Journal of Aircraft*, Vol. 46, No. 2, 2009, pp. 355–368. doi:10.2514/1.34957

[49] Pirzadeh, S. Z., "Advanced Unstructured Grid Generation for Complex Aerodynamic Applications," *AIAA Journal*, Vol. 48, No. 5, 2010, pp. 904–915. doi:10.2514/1.41355

[50] Frink, N., "Strategy for Dynamic CFD Simulation on SACCON Configuration," AIAA Paper 2010-4559, June 2010.

[51] Murphy, P. C., Klein, V., Frink, N. T., and Vicroy, D. D., "System Identification Applied to Dynamic CFD Simulation and Wind Tunnel Data," AIAA Paper 2011-6522, Aug. 2011.